High-Resolution Simulation of Hurricane Bonnie (1998). Part II: Water Budget

Scott A. Braun

Laboratory for Atmospheres, NASA/Goddard Space Flight Center, Greenbelt, MD

submitted to

Journal of the Atmospheric Sciences

March 15, 2004

Corresponding Author: Dr. Scott A. Braun, Mesoscale Atmospheric Processes Branch, NASA/GSFC, Code 912, Greenbelt, MD 20771. Scott.A.Braun@nasa.gov.

Popular Summary for

"High-Resolution Simulation of Hurricane Bonnie (1998). Part II: Water Budget"

Scott A. Braun

submitted to the *Journal of the Atmospheric Sciences*

Hurricanes are well known for their strong winds and heavy rainfall, particularly in the intense rainband (eyewall) surrounding the calmer eye of the storm. Outside of the eyewall, the hurricane precipitation is dominated by generally lighter and more horizontally uniform rainfall, although typically narrow rainbands with some embedded thunderstorms will be present. Much of the moisture that eventually condenses within the hurricane's clouds to form precipitation comes from transport of environmental water vapor in towards the eyewall in the strong inflow layer near the surface. Additional moisture is supplied by evaporation from the ocean surface. Some past studies have estimated that the amount of vapor evaporated from the ocean surface is just a very small percentage of that carried inward by the inflow while other studies have suggested that the ocean source of moisture becomes significant when you account for how much moisture is added along the path of the inflowing air. Several important questions are addressed in this study including

- How much of the water supplied to the storm comes from evaporation from the ocean?
- How much of the precipitation falling outside the eyewall originates in the eyewall?
- What are the causes of precipitation forecast errors?

This study uses a sophisticated numerical forecast model to simulate Hurricane Bonnie, which occurred in late August of 1998 during a special NASA field experiment designed to study hurricanes. Although the simulation produces too much rainfall (too large of a rain area and too intense) compared to observations from the NASA Tropical Rainfall Measuring Mission satellite, the overall structure of the simulated storm is quite good. The simulation results suggest answers to the above questions as follows:

- The water evaporated from the ocean surface is indeed just a small percent of that transported inward near the surface or condensed in clouds. The overestimated importance of surface evaporation in some past studies was likely caused by their underestimation of the inflowing moisture.
- Only a few percent of the rainfall outside of the eyewall actually comes from the eyewall. However, the eyewall provides large numbers of small ice seeds that can then grow into larger ice particles as they fall to the surface.
- The analysis suggests that the precipitation errors in this simulation are not necessarily caused by the representation of cloud physical processes (as often assumed) but instead may result from poor representation of the physics of the planetary boundary layer (the layer closest to the earth's surface that is affected by surface friction).

Abstract

The Pennsylvania State University-National Center for Atmospheric Research mesoscale model MM5 is used to simulate Hurricane Bonnie at high resolution (2-km spacing) in order to examine budgets of water vapor, cloud condensate, and precipitation. Virtually all budget terms are derived directly from the model (except for the effects of storm motion). The water vapor budget reveals that a majority of the condensation in the eyewall occurs in convective hot towers, while outside of the eyewall most of the condensation occurs in weak updrafts, indicative of a dominance of stratiform precipitation processes. The ocean source of water vapor in the eyewall region is only a very small fraction of that transported inward in the boundary layer inflow or that condensed in the updrafts. In contrast, in the outer regions, the ocean vapor source is larger owing to the larger area, counters the drying effect of low-level subsidence, and enhances the moisture transported in toward the eyewall. In this mature storm, cloud condensate is consumed as rapidly as it is produced. Cloud water peaks at the top of the boundary layer and within the melting layer, where cooling from melting enhances condensation. Unlike squall lines, in the hurricane, very little condensate produced in the eyewall convection is transported outward into the surrounding precipitation area. Most of the mass ejected outward is likely in the form of small snow particles that seed the outer regions and enhance stratiform precipitation development through additional growth by vapor deposition and aggregation.

In addition, artificial source terms for cloud and precipitation mass associated with setting negative mixing ratios, produced as a result of numerical advection errors, to zero are described. Although small at any given point and time, the cumulative effect of these terms contributes an amount of mass equivalent to 13% of the total condensation. Thus, these terms

must be accounted for to balance the model budgets and the results suggest the need for improved model numerics.

1. Introduction

The total heat content of normal tropical air, if raised by undilute ascent within cumulus towers, is insufficient to generate a warm core capable of reducing the surface pressure below ~1000 mb (Riehl 1954, Palmen and Riehl 1957, Malkus and Riehl 1960, Kurihara 1975). As suggested by Riehl (1954) and Palmen and Riehl (1957), for a hurricane to develop, a local heat source must exist to increase the equivalent potential temperature, θ_e, above normal surface air values of approximately 350 K. This heat source occurs as a result of surface fluxes of latent, and to a lesser extent, sensible heat from the ocean (Byers 1944).

Malkus and Riehl (1960) developed a dynamic model of the inflow layer and estimated the ratio of the moisture source from the ocean to the net horizontal moisture import to be less than 10%. While the moisture added to the atmospheric boundary layer is only a small fraction of the latent heat released within the cumulus towers or that carried inward by radial inflow, it is critical for the generation and maintenance of hurricanes (Palmen and Riehl 1957, Malkus and Riehl 1960, Riehl and Malkus 1961, Kurihara 1975, Hawkins and Imbembo 1976, Zhang et al. 2002). Malkus and Riehl (1960) emphasized that it is not the total amount or rate of condensation that is important for storm maintenance, but the heat content, or θ_e, at which the release occurs.

Kurihara (1975) examined budgets of a simulated axisymmetric hurricane. The dominant terms in the vapor budget were the total advection (horizontal plus vertical) and the latent heating. The total advection consisted of strong horizontal flux convergence of moisture at low levels and upward transport at mid levels. The water supplied by moisture convergence and evaporation was almost completely removed by condensation. An area of negative advection in outer regions in the boundary layer caused by subsidence of dry air was partially offset by evaporation from the ocean, similar to the findings of Ooyama (1969). Kurihara's (1975) volume-integrated budgets, computed out to 500 km, showed that evaporation from the surface was approximately 20 and 25% of the condensation and total advection, respectively. However, when the domain was restricted to the inner-core region, evaporation was negligible compared to either condensation or advection. Evaporation in the outer region supplied latent energy to the subsiding air and eventually contributed to the larger horizontal flux convergence of moisture into the inner area. Although small, if evaporation in the inner core was suppressed, Kurihara showed that the θ_e of the inflowing air could not be raised. Thus, the negligible amount of

evaporation was crucial to the energetics.

Hawkins and Embembo (1976) computed a water vapor budget for an intense Hurricane Inez (1966). While they found that the ocean source of water vapor was typically only about 6-13% of the horizontal transport into each 10-kilometer increment from the center to 50 km radius, they suggested that the cumulative input from the ocean surface within 50 km was comparable to the horizontal transport near the eyewall. A similar study of a much weaker storm by Hawkins and Rubsam (1968) produced comparable results, but with an even larger contribution from the ocean surface relative to horizontal transport as a result of much weaker radial inflow.

Zhang et al. (2002) computed thermodynamic budgets for a 6-km grid simulation of Hurricane Andrew (1992) and expressed the transport in advective form rather than in flux form. In this framework, horizontal advection tended to transport drier air into the core in the boundary layer and moist air from the eye to the eyewall within the low-level outflow above the boundary layer. They showed that the horizontal advective contribution was small compared to vertical advection in the eyewall. While technically correct, it may give the impression that the inflow dries out the core while, in fact, because of the rapidly decreasing area with decreasing radius, the horizontal moisture convergence moistens the core and provides the bulk of the moisture to the eyewall.

Few studies of the condensed water budget have been conducted for hurricanes. Marks (1985) estimated that 60% of inner-core region rainfall (radius r<110 km) of Hurricane Allen (1980) fell within stratiform rain areas and that the water vapor convergence into the eyewall was more than twice the volumetric rainfall. Gamache et al. (1993) suggested that this result indicated that a significant amount of condensate produced in the eyewall was ejected outward into the surrounding stratiform precipitation area, but noted that considerable uncertainty exists about the amount of condensate actually ejected outward. Marks and Houze (1987) divided a hurricane into two regions, the eyewall and the outer stratiform precipitation area, analogous to tropical squall lines, in which 30-50% of precipitation falls out as stratiform rain (Gamache and Houze 1983, Churchill and Houze 1984). They estimated that 62% of the rain within the radar volume (r<40 km) fell in the stratiform region (r> 20 km). Using representative assumed values of vertical motion, air density, water vapor content at cloud base, outflow speed, and water content differential between the eyewall and outer stratiform area, they estimated that the

condensation in the stratiform region was approximately three times the mass transported outward from the eyewall, about an order of magnitude larger than estimated for tropical squall lines. This result suggested that in-situ production of water dominated.

Gamache et al. (1993) produced a more detailed water budget using dual-Doppler data collected within Hurricane Norbert (1984). Their analysis domain extended outward only to about 40 km from the center and included the eyewall and a small portion of the outer precipitation area. They found little total outflow of condensate from the eyewall, consistent with weak radial flow in Norbert at the analysis time. Although the total outflow of condensate was small, they suggested that more intense outflow of ice was possible because of asymmetries in the radial flow, which favored inflow (outflow) on the rear (front) side of the storm relative to its motion. The upper-level inflow in the rear quadrants prevented lighter precipitating particles from being detrained immediately from the eyewall, instead being carried slowly inward until they reached the front of the storm. Upon encountering the outflow there, the particles were then ejected outward into the surrounding stratiform precipitation area. They suggested that this localized outflow from the eyewall thus contributed significant amounts of ice for development of the stratiform precipitation.

Gamache et al. (1993) also calculated a water vapor budget for Norbert. Based upon a large value of the estimated vapor diffusion across the bottom boundary of their budget volume (~500 m), they concluded that about 40% of the vapor converging into the volume had evaporated from the sea surface. This amount is significantly larger than found in previous studies. They also estimated that most of the horizontal water vapor convergence occurred below 500 m in the boundary layer, but suggested that budgets for storms with deeper inflow were necessary to determine if the dominance of the boundary layer moisture convergence in Norbert is typical of other storms.

In this study, we compute budgets of both water vapor and total condensed water from a high-resolution simulation of Hurricane Bonnie (1998), with virtually all budget terms written directly from the model, thereby avoiding many of the gross approximations necessary in previous budget studies. Since some disagreement exists between studies suggesting that the ocean vapor source is nearly negligible in the inner core (Palmen and Riehl 1957, Malkus and Riehl 1960, Kurihara 1975) to others suggesting that the cumulative effect is substantial (Hawkins and Rubsam 1968, Hawkins and Imbembo 1976, Gamache et al. 1993), the simulation

results are used to quantify the contribution of the ocean source of vapor relative to the radial import of vapor. In addition, since few condensed water budgets have been examined, complete budgets for both cloud and precipitation hydrometeor mass are calculated with some emphasis on the amount of condensate advected from the eyewall to the outer precipitation region. Furthermore, the condensate budget is used to quantify the extent to which total water is conserved by the model, an issue that may be more important than previously believed.

2. Simulation and analysis description

a. Simulation description

The model used in this study is the Pennsylvania State University—National Center for Atmospheric Research (PSU—NCAR) non-hydrostatic fifth generation mesoscale model (MM5 V3.4; Dudhia 1993; Grell et al. 1995). Because of computational limitations, the simulation was conducted in two steps. First, a coarse-resolution simulation was performed using an outer mesh with 36-km horizontal grid spacing, 91×97 grid points in the x and y directions, respectively, and 27 half-σ levels, where σ is the model terrain following coordinate. A second inner mesh with 12-km horizontal grid spacing consisted of 160×160 grid points. The simulation was started at 1200 UTC 22 August 1998 and run for 36 hours, with model output saved every hour. Physics options for the coarse-grid simulation included a modified version of the Blackadar planetary boundary layer scheme in which surface roughness calculations for temperature and moisture follow Garratt (1998) and Pagowski and Moore (2001). Cloud processes were represented by the Grell cumulus parameterization scheme and the Goddard Cumulus Ensemble model cloud microphysics. Shortwave radiative processes were represented by the cloud-radiation scheme of Dudhia (1989) while longwave radiation used the Rapid Radiative Transfer Model of Mlawer et al. (1997) and were calculated every five minutes.

Initial and boundary conditions were obtained from 12-hourly global analyses from the European Center for Medium-Range Weather Forecasts archived at NCAR. Analysis fields, including temperature, relative humidity, geopotential height, and winds at mandatory pressure levels and with horizontal resolution of 2.5° were interpolated horizontally to model grid points. These interpolated analyses were refined by adding information from standard twice-daily rawinsondes and three-hourly surface and buoy reports using a Barnes objective analysis technique (Manning and Haggenson 1992). Final analyses were then interpolated to the model

vertical levels. Because the large-scale analysis did not contain an adequate representation of the initial hurricane vortex, a bogusing technique using four-dimensional variational data assimilation developed by Zou and Xiao (2000) and Xiao et al. (2000) and modified by Pu and Braun (2001) was used. See Pu and Braun (2001) for more details on the methodology.

A high-resolution simulation was conducted by using 1-h output from the 36- and 12-km grids to provide initial and boundary conditions for a 6-km grid (225×225×27 grid points) and 2-km grid (226×226×27) starting at 6 h into the forecast to allow for some model spin up on the 12-km grid. The high-resolution grids were run for 30 hours until 0000 UTC 24 August. The 2-km grid was moved hourly to keep it centered on the storm. Model physics were identical to the coarse-grid simulation except that no cumulus parameterization scheme was used and model output was saved every 15 minutes. For the water budget calculations, the simulation was repeated for 1 h between 24-25 h with all terms from the budgets written directly from the model every 3 minutes. Only the contribution associated with the storm motion is calculated offline (see section 3). Braun et al. (2004) focused on the period between 24-30 h, with model output every 3 min in order to resolve the evolution of individual updrafts, and placed this period within the context of the overall evolution of the simulated storm.

The storm center was determined, as in Braun (2002), at every model output time using the pressure field at the lowest model level. The technique uses the horizontal distribution of pressure to determine an approximate geometric center of the pressure field. Storm motion was then computed from the identified center locations. To compute the time-averaged fields, model output fields were transferred to a grid in which the storm's center was fixed with respect to both height and time.

The equivalent radar reflectivity factor for any hydrometeor category, Z_x, is computed following Fovell and Ogura (1988) as $Z_x = 720\alpha\kappa N_{0x}\lambda_x^{-7}$, where α is the ratio of the backscattering coefficients for the reflecting particles and water (0.213 for snow and graupel, 1 for rain), $\kappa=10^{18}$, N_{0x} is the intercept parameter of the particle size distribution, λ_x is the slope of the size distribution, $\lambda_x = \left(\pi\rho_x N_{0x}/\rho q_x\right)^{1/4}$, ρ and ρ_x are the densities of air and the hydrometeor type (rain, snow, graupel), respectively, and q_x is the hydrometeor mixing ratio. The reflectivity is expressed in decibels, or dBZ, where $\mathrm{dBZ} = 10\log_{10}\left(Z_r + Z_s + Z_g\right)$ and the subscripts r, s, and g indicate rain, snow, and graupel, respectively. For this simulation, $N_{0r}=8\times10^6$ m^{-4}, $N_{0s}=4\times10^6$ m^{-4}, $N_{0s}=4\times10^6$ m^{-4}, $\rho_s=0.1$ g cm^{-3}, and $\rho_g=0.23$ g cm^{-3}.

b. Simulated structure and validation

Braun et al. (2004) provide a more detailed validation of the Bonnie simulation and discussion of the factors influencing the distribution of vertical motion in the eyewall. They showed that the simulation reproduces the intensity and intensity change well, with the exception that the simulated central pressure deepened somewhat more than observed in the last 12 hours of simulation and that the model maximum winds tended to be somewhat too strong. The simulated track error was typically less than 100 km except in the final hours during which it increased to approximately 120 km. The simulated precipitation structure (Fig. 1c) was very similar to that observed at 1800 UTC 22 August 1998 by the Tropical Rainfall Measurement Mission (TRMM) precipitation radar (Fig. 1a). The precipitation structure changed little during the simulation whereas the observed structure became much more asymmetric by 24 August (Fig. 1b). As discussed in Braun et al. (2004), the model precipitation did not achieve the high degree of asymmetry in part because the model did not strengthen the environmental vertical wind shear over the storm as observed.

Here, we focus more on comparison of the reflectivity distributions between the simulation and observations in order to evaluate the simulated microphysical structure. Comparison of Fig. 1c with Figs. 1a and 1b suggests that too much rain water mass occurs in the simulation. All levels can be examined simultaneously by comparing contoured frequency by altitude diagrams (CFADS, Yuter and Houze 1995) of reflectivity in Fig. 2. The CFADS are obtained by computing histograms of reflectivity (from 15 to 60 dBZ) at each level and normalizing by the number of grid points with reflectivity greater than 15 dBZ. This lower limit

is chosen because the TRMM radar lacks the sensitivity to detect reflectivities less than this value. The TRMM CFAD (Fig. 2a) shows a relatively narrow distribution, particularly in the ice region. Below the melting level (~5 km), reflectivities range from 15 to about 50-55 dBZ (60 dBZ near the surface), but are most often between 30-37 dBZ. Above the melting level, reflectivities range from 15-36 dBZ, with a few values > 40 dBZ just above the melting level, but most values lie between 15-25 dBZ. In contrast, the simulated reflectivities (Fig. 2b) exhibit a much broader distribution with values in the rain region more frequently above 45-50 dBZ and extreme values near 60 throughout the rain layer. In the ice region, reflectivities >30 dBZ are very frequent with extrema up to 50 dBZ. Between 6-12 km, reflectivities are often about 10-20 dBZ larger than observed. If it is assumed that the intercept parameters are representative of those in actual hurricanes, then clearly the model is producing too much precipitation mass at all levels. One is often inclined to lay blame on the cloud microphysical parameterization for such errors. In fact, substantial reductions in reflectivity are possible if the intercepts of the size distributions are increased by an order of magnitude. However, as Braun and Tao (2001) suggest, other physical processes such as those in the boundary layer can have substantial impacts on precipitation fields. Environmental humidity errors may also have an impact. While determination of the exact causes of error is beyond the scope of this study, the water budget results in section 4 may provide some clues regarding possible sources of error.

Next, we examine the simulated structure of Bonnie to provide context for the budget calculations in section 4. Figure 3 displays the horizontal variation of the precipitation and kinematic structures at several levels using 1-h averaged fields of reflectivity, radial velocity, and vertical velocity. Near the surface (Fig. 3a), the heaviest precipitation is concentrated on the northeastern side of storm as a result of asymmetries induced by the environmental wind shear (Rogers et al. 2003, Zhu et al. 2003, Braun et al. 2004). Two regions of very high reflectivities (> 45 dBZ) are apparent, one in the eyewall and the other in a principal rainband near a radius of r = 130 km. A much weaker band, more detectable in the vertical velocity fields, lies in between the eyewall and principal rainband and will be referred to as the intermediate band. Radial velocities show low-level inflow surrounding the storm with weak outflow within the eye. The strongest inflow occurs radially just outside the northeastern eyewall and just outside the principal rainband.

At 2.7 km (Fig. 3b), the strongest upward motion is on the northeastern side of the

eyewall as well as along the inner edge of the principal rainband, while very weak upward motion occurs within the intermediate band. At 6.8 km (Fig. 3c), the strongest eyewall vertical motion shifts to the eastern side. As mentioned in Braun et al. (2004), this shift occurs because of changes in the storm-relative environmental flow with height. Specifically, within the boundary layer, the strongest inflow is on the northeastern side and low-level convergence there produces upward motion at the top of the boundary layer. Above the boundary layer, inflow and convergence at low levels and outflow and divergence at upper levels (Fig. 3d) on the southeastern side of the eyewall lead to deep upward motion there. The upward motion extends around the southern side to the western side of the eyewall and is associated with a distinct area of upper-level outflow (Fig. 3d). In the principal band, stronger upward motion is concentrated in two areas along the band, with the rest of the band exhibiting much weaker upward motion. The intermediate band is more distinct at mid-to-upper levels than at lower levels with a single core of more intense upward motion. Downward motion tends to dominate the northwestern side of the eyewall.

At upper levels (Fig. 3d), a well-defined asymmetry of radial velocity is present with inflow on the northwestern side and outflow generally on the southeastern side just outside of the eyewall. This asymmetry is associated with a northwesterly storm-relative environmental flow that occurred as the storm approached an upper-level trough (Zhu et al. 2003, Braun et al. 2004). In the eyewall, inflow occurs on the northeastern side and outflow on the southwestern side. This result means that hydrometeors ejected from convection on the northeastern side of the eyewall are not detrained outward unless they are advected around to the southern side before falling appreciably, similar to the findings of Gamache et al. (1993).

The vertical structure of the hydrometeor and kinematic fields is further explored in Fig. 4, which shows west-to-east cross sections through the center of the storm. The eastern side of Bonnie shows deep ascent in the eyewall (Fig. 4a). The principal rainband is associated with a strongly outwardly sloping region of ascent composed of multiple updraft cells of increasing depth and altitude. This structure represents a slice through a gap between the two elongated cells in the band (Figs. 3b, 3c), but the azimuthally averaged vertical motion field (Fig. 5c) suggests that the slope may be characteristic of the band. Mid-to-upper level ascent occurs in the intermediate band. Cloud liquid water (Fig. 4b) is most concentrated in the updrafts with peak values often found in the melting layer. Inflow on the eastern side (Fig. 4c) is limited to levels

below 4 km, becoming shallower closer in to the eyewall where the inflow is confined to the lowest 1 km. Weak outflow occurs in the eyewall and intermediate band, sloping upward with increasing radius. Stronger (>10 m s^{-1}) and deeper outflow occurs outward of the principal rainband.

On the western side of the storm, upward motion is generally confined to upper levels and occurs above the convergent interface between strong upper-level outflow and inflow immediately beneath the cloud ice layer (c.f., Figs. 4b, 4c). Downward motion generally occurs beneath this interface so that the upper inflow region descends within the eyewall. A deep, but weak, reflectivity core is associated with the eyewall, while further outward the reflectivity structures are quite shallow. Even though low-level updrafts are weak or nearly absent, substantial cloud water is present with relative maxima in the melting layer and at the top of the boundary layer. Low-level inflow on this side is restricted to the boundary layer with weak outflow at the top of the boundary layer.

The azimuthally averaged structure is shown in Fig. 5. The average tangential winds (Fig. 5a) reach approximately 56 m s^{-1} near the top of the boundary layer with the radius of maximum wind near 50 km. Radial velocities (Fig. 5b) depict inflow concentrated in the boundary layer with little inflow occurring above the boundary layer. The primary outflow occurs above 12 km. Weaker outflow is present at the top of the boundary layer in the eyewall as well as radially outward from the principal band (r > 150 km) between 7-10 km above mean sea level (MSL). Maximum average ascent (Fig. 5c) in the eyewall is ~1.4 m s^{-1}, with the eyewall sloping outward from 40 km near the surface to 52 km near 10 km MSL. Strongly outwardly sloping regions of weaker ascent occur between r = 120-200 km associated with the principal rainband and between 70-110 km associated with the intermediate band.

The water vapor field (Fig. 5d) shows large positive deviations from the domain averaged value in the eye and the eyewall and negative values outside the eyewall. The air dries rapidly radially outward from the principal band, suggesting perhaps that the rainband, at least to some extent, shields the eyewall from the drier environmental air. Maximum cloud water occurs in the eyewall (Fig. 5b) and, in both the eyewall and outer regions, cloud water peaks in the vertical near the top of the boundary layer and within the melting layer. Condensation is enhanced in this latter layer as a result of cooling by melting that attempts to or succeeds in producing a near 0°C

isothermal layer depending on whether sufficient condensation warming occurs to remove the isothermal layer (discussed in more detail in section 4).

The precipitation mixing ratios (Fig. 5f) show peak rain values greater than 1.5 g kg^{-1}, graupel values greater than 1.8 g kg^{-1} just above the melting level, and snow values greater than 1.5 g kg^{-1} a few kilometers above the graupel maximum. A weak secondary maximum occurs between 125-175 km associated with the principal band. Most of the graupel occurs beneath the outflow region so that little outward advection of graupel occurs. In contrast, the upper portion of the heavy snow region coincides with the outflow so that much of the outward precipitation mass flux is associated with smaller detrained snow particles.

3. Budget formulation

Although the full model equations are used in the calculation of budget terms, for discussion we use more simplified forms. The equations for water vapor, total cloud content (cloud liquid water and ice) and total precipitation content (rain, snow, and graupel) may be written as follows:

$$\frac{\partial(\rho q_v)}{\partial t} = -\nabla\cdot(\rho q_v V') - \frac{\partial(\rho q_v w)}{\partial z} + \rho q_v\left(\nabla\cdot V' + \frac{\partial w}{\partial z}\right) - \rho(C-E) + \rho B_v + \rho D_v \tag{1}$$

$$\frac{\partial(\rho q_c)}{\partial t} = -\nabla\cdot(\rho q_c V') - \frac{\partial(\rho q_c w)}{\partial z} + \rho q_c\left(\nabla\cdot V' + \frac{\partial w}{\partial z}\right) + \rho(Q_{c+} - Q_{c-}) + \rho B_c + \rho D_c + \rho Z_c \tag{2}$$

$$\frac{\partial(\rho q_p)}{\partial t} = -\nabla\cdot(\rho q_p V') - \frac{\partial(\rho q_p w)}{\partial z} + \rho q_p\left(\nabla\cdot V' + \frac{\partial w}{\partial z}\right) + \frac{\partial(\rho q_p V_T)}{\partial z}$$

$$+ \rho(Q_{p+} - Q_{p-}) + \rho D_p + \rho Z_p \tag{3}$$

where q_v, q_c, and q_p are the water vapor, cloud, and precipitation water mixing ratios, respectively; V' is the storm-relative horizontal air motion; w and V_T are the vertical air and hydrometeor motion; Q_{c+}, Q_{c-}, Q_{p+}, and Q_{p-} are the cloud and precipitation microphysical sources (+) and sinks (–); C is the condensation and deposition; E is the evaporation and sublimation; $C - E = Q_{c+} - Q_{c-} + Q_{p+} - Q_{p-}$; B_v and B_c are the contributions from the planetary boundary layer parameterization to vapor and cloud; D_v, D_c, and D_p are parameterized turbulent diffusion terms for vapor, cloud, and precipitation; and Z_c and Z_p are artificial source terms associated with setting negative mixing ratios (caused by errors associated with the finite differencing of the advective terms) to zero, i.e., mass is added to eliminate negative mixing ratios. Each term is written directly from the model except for the storm motion contribution in the horizontal advective flux terms. The storm motion contribution is calculated offline using the exact same code used for horizontal advection in the model, but with the storm motion substituted for the air motion.

Azimuthal, vertical, and volume averages are computed using

$$\overline{[\,]} = \int_0^{2\pi} [\,]\,\partial\lambda \tag{4}$$

$$\hat{[\,]} = \int_{\sigma_s}^{\sigma_t} [\,]\,\partial\sigma \tag{5}$$

$$\overline{\overline{[\,]}} = \int_{\sigma_s}^{\sigma_t}\int_0^{2\pi}\int_{R_1}^{R_2} [\,]\, r\,\partial r\,\partial\lambda\,\partial\sigma \tag{6}$$

where λ is azimuth in a cylindrical coordinate system aligned with the storm center, σ_s and σ_t are the lowest and upper-most half-σ levels of the model domain, and R_1 and R_2 are the radial limits of integration. If the horizontal advective flux terms are expressed in cylindrical coordinates,

$$-\frac{\partial(\rho q_x U)}{\partial x} - \frac{\partial(\rho q_x V)}{\partial y} = -\frac{1}{r}\frac{\partial(r\rho q_x u)}{\partial r} - \frac{1}{r}\frac{\partial(\rho q_x v)}{\partial \lambda}, \tag{7}$$

where q_x is either q_v, q_c, or q_p; r is radius; U and V are the Cartesian grid storm-relative horizontal velocities in the x and y directions; and u and v are the storm-relative radial and tangential winds; then the azimuthally averaged horizontal advective flux is simply that associated with radial transport. If the horizontal advective flux is averaged over the cylindrical volume from the center to some radius R, then the result gives the net radial transport across the boundary at R. The surface precipitation flux is given by the vertical integral of the precipitation fallout term in (3).

Water vapor and condensed water budgets are calculated for an inner region enclosing the eye and eyewall and an outer region generally consisting of convective rainbands and stratiform precipitation. Each term in (1-3) is averaged following (6) from r=0 to R_{in} for the inner region and R_{in} to R_{out} for the outer region. All values are then normalized by the total condensation between r=0 and R_{out}. Naming conventions for each of the budget terms to be presented in Fig. 13 are listed in Table 1. The values of R_{in} and R_{out} are set to 70 and 200 km, respectively.

4. Budget results

a. Water vapor budget

The azimuthally averaged water vapor budget fields are displayed in Fig. 6. The largest individual terms are the horizontal and vertical water vapor flux divergence terms (Fig. 6b, 6d) that are typically an order of magnitude larger than other terms. However, they largely cancel and their sum (Fig. 6f) is nearly equal to but opposite the net condensation (Fig. 6e). The horizontal transport is characterized by strong moisture convergence in the eyewall boundary layer and moisture divergence above the boundary layer associated with low-level outflow. The vertical moisture flux divergence field shows strong upward transport of moisture from the boundary layer into the eyewall cloud. The condensation field (Fig. 6a) shows peak values in the

eyewall between 2-4 km MSL, decreasing fairly rapidly above the melting level. Weaker secondary maxima coincide with the outer rainbands. The evaporation field (Fig. 6c) is much weaker, with maximum values just outward of the eyewall. The divergence term (Fig. 6g) is generally negligible except in the eyewall where it produces weak drying. Consistent with earlier studies (Ooyama 1969, Kurihara 1975), drying of the boundary layer in the outer regions associated with the vertical moisture flux divergence is largely compensated by the moistening effect of boundary layer processes (Fig. 6h).

Riehl and Malkus (1961) estimated the vertical mass and heat fluxes within cumulus towers, or hot towers, in hurricane Daisy (1958) and found that the percentage of each increases as the center is approached. The hot towers accounted for a majority of the mass flux in the eyewall and of the heat flux within a broader portion of the inner-core region. Jorgensen et al. (1985), using flight-level in-situ data, and Braun (2002), using a high-resolution simulation of a hurricane, found that updraft cores tend to occupy a small percentage of the eyewall area, yet account for a majority of the vertical mass flux in the eyewall. The statistical distribution of vertical motion in the eyewall can be examined to determine the percentage of the eyewall area and condensation associated with convective updrafts. Histograms of updraft area and condensation rate as a function of vertical velocity are computed for a 40 km-wide radial band (30-70 km radius) for each model level using a vertical velocity bin size of 0.5 m s^{-1}. The 40-km-wide band just encloses the ensemble of updrafts occurring at all levels in the eyewall during the 1-h period considered. The shaded contours in Fig. 7a show the cumulative percentage of the eyewall area occupied by updrafts less than the indicated value. Similarly, the solid contours indicate the contribution to the total eyewall condensation produced in updrafts less than the indicated value. The figure indicates that updrafts greater than 2 m s^{-1} occupy somewhat less than 10% of the eyewall area at lower to middle levels and 20% at upper levels. Updrafts greater than 4 m s^{-1} generally occupy less than 5% of the eyewall area, in general agreement with the results of Braun (2002). Although these updrafts account for only a small percentage of the eyewall area, they produce a majority of the total condensation occurring within the eyewall. Updrafts greater than 2 m s^{-1} produce 75% of the total condensation in the eyewall while updrafts greater than 4 m s^{-1} account for half of the condensation. As shown in Braun et al. (2004), updrafts >2 m s^{-1} tend to be associated with deep updraft towers rather than more widespread areas of ascent so that much of the eyewall condensation is associated with hot towers. In the outer precipitation

area (70-200 km), the percentage of the area with updrafts greater than 2 m s^{-1} decreases significantly, largely because of the much larger total area, with such updrafts occupying only about 5% of the area. Updrafts > 4 m s^{-1} occupy <1% of the area. Unlike their larger contribution in the eyewall region, updrafts greater than 4 m s^{-1} contribute only ~10-20% of the condensation. The smaller contribution of stronger updrafts is indicative of the larger role of stratiform precipitation processes outside of the eyewall.

b. Condensed water budget

In this section, the budget for total condensed water is subdivided into its cloud (non-precipitating) and precipitating components. Azimuthally averaged fields for the most important terms in the cloud budget are shown in Fig. 8. The total source of cloud (condensation, shown in Fig. 6a) is nearly canceled by the total sink (Fig. 8a) associated with evaporation, auto conversion, and collection of cloud by rain, snow, and graupel so that the cloud mass is consumed about as fast as it is produced. Unlike the water vapor field, the advective transports are much smaller than the source/sink terms. Outward transport (Fig. 8b) of cloud occurs in the low-level outflow in the eyewall, with weaker outward transport aloft. Net production (Fig. 8c) of cloud is positive in the boundary layer and along the inner edge of the eyewall and negative above the boundary layer, especially within or just above the melting layer. The vertical transport (Fig. 8d) generally has the opposite pattern. The layer of positive vertical transport near the melting level is produced by upward advection of the melting-layer cloud liquid water (Fig. 5e) while the negative values of net production are likely caused by collection of the lofted cloud by precipitating hydrometeors. The boundary layer parameterization makes a small contribution to cloud near the surface in the inner-core region.

As mentioned previously, the cloud water in the melting layer is produced by condensation in the updrafts penetrating through the layer and Fig. 8 shows that this water is carried upward and then scavenged by the precipitating hydrometeors. Condensation is enhanced in the melting layer by cooling associated with melting precipitation. This melting can cause development of a near 0°C isothermal layer that, when condensation is weak, is readily apparent in the temperature profiles in precipitating regions, or if condensation is sufficiently strong, is immediately removed by heating. In the microphysical code, the cooling from melting is applied to the temperature field immediately prior to the condensation calculation and so the

production and destruction of the isothermal layer can be entirely transparent at the end of the model time step.

The finite-difference representation of advective processes (2nd order centered differencing in space, leap-frog in time) can cause small negative mixing ratios near cloud edges, generally on the upstream side, and these negative mixing ratios are systematically set to zero, thereby resulting in an artificial source of water. The mass added at any grid point is small, but when summed over the model domain and over every time step, it can become significant. The last panel in Fig. 8 shows the water mass added by setting negative mixing ratios to zero. Since this "correction" occurs just prior to calculation of the microphysical processes, the added cloud water leads to additional evaporation and collection so that the net microphysical production (Fig. 8c) is generally negative.

Azimuthally averaged fields for the precipitation budget are shown in Figs. 9 and 10. The sources and sinks of rain, graupel, and snow are presented in Fig. 9, while the net production, horizontal transport, net vertical flux (advective plus fallout terms), and artificial source term for total precipitation are shown in Fig. 10. Below 4-5 km, rain production (Fig. 9a) associated with warm-rain processes is largest in the eyewall. Rain production from melting ice is also largest in the eyewall, but is also spread throughout the storm. Most of the melting of ice is associated with graupel (Fig. 9d) since the sink of snow (Fig. 9f) occurs primarily above the melting level in association with collection by graupel (Fig. 9c) and sublimation. The rain sink is associated with evaporation in downdrafts within or just outside of the eyewall and freezing or collection of rain by cloud and precipitation ice in the eyewall and principal band. Snow production is likely dominated by deposition and collection of cloud ice.

The net production of precipitation (Fig. 10a) is nearly identical to, but opposite in sign from, the cloud mass sink (Fig. 8a). Some outward transport (Fig. 10b) from the eyewall occurs above the boundary layer, while inward transport occurs within the boundary layer. The net vertical advective flux and precipitation fallout (Fig. 10c) is mostly negative and largely balances production. The addition of precipitation mass to offset negative mixing ratios (Fig. 10d) is strongest in the eyewall melting layer, with a secondary maximum on the inner edge of the eyewall. A more detailed discussion of this artificial source term is presented in section 4d.

Next, the horizontal distributions of some of the budget quantities are examined through their vertically integrated distributions. The vertically integrated condensation field (Fig. 11a)

shows that most of the condensation occurs within the eyewall and principal rainband on the eastern side of the storm, with weaker condensation in between. In contrast, the integrated evaporation (Fig. 11b) is somewhat more evenly distributed. The maximum evaporation on the northeastern side occurs in downdrafts just radially outward from the condensation peak. Additional eyewall evaporation occurs in the relatively precipitation-free area on the western side of the storm and in the area of the principal band where dry environmental air tries to enter the inner-core region (Fig. 5d).

The vertically integrated rain fallout (Fig. 11c) is equivalent to the rainfall flux at the surface. Interestingly, the rainfall maximum is located only slightly (a few tens of kilometers at most) downwind of the condensation peak. The lack of substantial azimuthal displacement of the precipitation from its source region to where it reaches the surface appears to be related to two factors in this case. The first factor is that much of the rain water production in the eyewall occurs in association with warm-rain processes. Figure 12a shows the vertically integrated source of rain, which strongly resembles the integrated condensation and fallout fields. The contribution of warm- versus cold-rain processes to the total production of rain may be estimated by assuming that all of the graupel sink is associated with melting (since sublimation of graupel is generally small) and adding the graupel sink to the rain source. The resulting warm-rain source and cold-rain source (graupel sink) are shown in Figs. 12b and 12c. It can be seen that total rainfall production is dominated by warm-rain processes. However, we note that some of this rain production is associated with rain that originally formed from melting ice and then subsequently collected cloud water as it fell to the surface. The contribution from melting is small in a vertically integrated sense since, although the melting rates are large (Fig. 9d), they are confined to a very shallow layer. The peak warm-rain generation is on the northeastern side of the eyewall where low-level upward motion (Fig. 3b) is maximum. Since condensation peaks at relatively low levels (Fig. 6a) and rain fall speeds are >5 m s^{-1}, the rainfall generated by warm-rain processes falls out fairly rapidly with relatively little azimuthal displacement. The second factor is that upward motion at upper levels is located on the eastern side of the storm (Fig. 3c), somewhat upwind of the low-level maximum. The integrated graupel source is maximum there (Fig. 12d). Graupel falls at a slower rate than rain, and from a higher level, so that rain water from melting graupel is advected further downwind than rain generated from warm-rain processes, but ends up reaching the surface on the northeastern side of the storm.

c. Volume integrated budgets

The volume integrated budgets of water vapor and total condensed water (cloud plus precipitation) are shown in Fig. 13. The storm is divided into two sections. The first is the eye and eyewall region that extends outward from the center to a radius that just encloses the top of the eyewall updraft and the low- to midlevel downdrafts (Fig. 5c, $r < 70$ km). The second region is the outer rain area from $r = 70$ to 200 km and includes the principal and intermediate rainbands. The values in Fig. 13 are normalized by the total condensation in the two regions (i.e. , over $r < 200$ km).

In the water vapor budget (Fig. 13a), the eyewall accounts for 20% of the total condensation, approximately one-third of which is evaporated. The bulk of the moisture is supplied by the net radial import, with 17.2 units supplied by the inflow primarily in the boundary layer and 4.7 units carried outward by the upper outflow. All other terms are small including the ocean source of vapor which is only ~4% of the low-level radial import of moisture. The vertical flux divergence term should be zero if the vertical velocity is zero at the top and bottom of the domain. However, the flux term at the lowest level is calculated at 40 m (the lowest half-σ level), where $\rho w q_v$ is very small but not necessarily zero. Because the upper boundary is not a rigid lid, $\rho w q_v$ can also be non-zero there.

Marks (1985) noted that in Hurricane Allen (1980) the moisture convergence into the eyewall was more than twice the volumetric rainfall. Gamache et al. (1993) suggested that although this estimate entails significant uncertainty, it suggests that a significant portion of the condensate produced is carried outward into the outer precipitation area. However, Fig. 13a suggests that not all of the moisture converged into the eyewall is carried outward in the form of condensate. A substantial amount may also be exported as vapor to moisten the surrounding area, an effect that is likely important for developing the stratiform precipitation area, particularly during the early stages.

Approximately 80% of the total condensation occurs in the outer region, of which approximately 45% is evaporated. Horizontal moisture import across the outer boundary is less than the condensation and an amount of vapor about an order of magnitude smaller is carried outward by the upper-level outflow. The outer-region boundary layer source of vapor is approximately 8% of the low-level moisture import across $r = 200$ km, but ~27% of the transport into the eyewall. As mentioned earlier, the ocean source of vapor in the inner region is only ~4%

of the inward transport across r = 70 km. These values of the ratio of the ocean source to the horizontal moisture import are consistent with Malkus and Riehl (1960) and Kurihara (1975), but are generally smaller than estimates by Hawkins and Rubsam (1968) and Hawkins and Imbembo (1975). From Fig. 20 of Hawkins and Rubsam, the ocean moisture source inside 80 km radius is estimated to be approximately 54% of the total moisture import below 600 mb and crossing that radius. However, the analysis included data from just five levels, the lowest at 900 mb (~989 m). Their diagnosed inflow was only 4-5 m s^{-1}, suggesting that the main inflow, likely below the 1-km level, was not included in their analysis. In Hawkins and Imbembo, the estimated ocean source inside of 50 km was approximately 25% of the transport across that radius. As in Hawkins and Rubsam, data from only five levels was available, the lowest at 950 mb (540 m). Although the inflow was stronger (approximately 15 m s^{-1}), an important contribution from the layer below 540 m was neglected. Gamache et al. (1993) estimated that the moisture convergence below 500 m can be significantly larger than that at higher levels, suggesting that the Hawkins and Rubsam and Hawkins and Imbembo budgets underestimated the total horizontal import and thus overestimated the ocean source contribution relative to the import.

Gamache et al. suggested that ~40% of the vapor converging into their budget volume was evaporated from the surface. This value may be excessively high for two reasons. First, they assumed that the radial wind below 500 m was the same as at that level. The model radial velocities actually increase toward the surface and, to the extent that this increase is characteristic of tropical cyclones, suggests that the moisture convergence below 500 m was underestimated. Second, their estimated vapor diffusion across the 500 m level was quite large and may result from the very large value of the eddy diffusivity (1500 m^2 s^{-1}) used in the retrieval algorithm in order to maintain computational stability. Eddy diffusivity values calculated from simulations of Hurricane Bob (1991) by Braun and Tao (2001) show azimuthally averaged values < 300 m^2 s^{-1} for four different parameterizations of the boundary layer.

The condensed water budget is shown in Fig. 13b. Again, eyewall condensation is approximately 20% of the total and about one-third is lost to evaporation. About 70 percent of the condensate falls to the surface as precipitation. The outward transport of condensate aloft is approximately 9% of the eyewall condensation, while about half of this amount is carried into the eyewall region by low-level inflow. While the outward transport is about 9% of the eyewall condensation, it represents only about 2% of the precipitation generation in the outer region.

Even though the amount of mass transported into the outer region is small, it is likely composed of a large number of small ice particles that seed the outer stratiform area. Subsequent growth of these particles by deposition and aggregation can significantly enhance the stratiform precipitation similar to the generation of secondary reflectivity maxima in the stratiform regions of squall lines (Smull and Houze 1985, Biggerstaff and Houze 1993, Braun and Houze 1994). Approximately 80% of the total condensation occurs in the outer region, with about 45% of the water lost to evaporation. Despite the evaporation, the precipitation efficiency (P/Cond) is approximately 65%, which is possible only because the artificial source term associated with setting negative mixing ratios to zero is about 13% of the condensation (this is true in the eyewall region as well).

d. The artificial water source

The volumetric budget indicated that although the mass added to offset negative mixing ratios is small at any grid point, the integrated addition of mass is about 13% of the total condensation. Next, we further explore this substantial, but artificial, water source. Figure 14 shows cross sections of the azimuthally averaged water fields as well as the sources of each hydrometeor type associated with setting negative mixing ratios to zero. Figure 15 shows the horizontal distribution of the vertically integrated water source for rain, graupel, and cloud water. Most of the added water mass in the eyewall comes from the cloud liquid water, rain, and graupel terms. The magnitude of the source term for cloud water is generally smaller than for rain or graupel, but is widespread throughout the cloud region (Figs. 14a, 15a). The cloud ice source is also small, but widespread on the underside of the anvil. In contrast, for rain and graupel, the sources are fairly localized in two regions, the melting layer and the region of strong horizontal gradient on the inner edge of the eyewall (Figs. 14b, 14c). Figure 15 shows that the rain and graupel sources are also concentrated in the eastern half of the eyewall as well as in portions of the outer rainbands while, again, the cloud water source is very widespread. For rain, the melting layer source is typically associated with vertical advection in downdrafts while for graupel the melting layer source is generally in the updrafts, consistent with negative mixing ratios being generated on the upstream side of advection of a sharp feature. The sources for rain and graupel along the inner edge of the eyewall are typically associated with horizontal advection in outflow such that negative mixing ratios occur on the upstream side. The source for

snow is very small and localized in the eyewall.

Table 2 shows a breakdown of the contributions of each hydrometeor category to the total artificial source term. In the eyewall region, 41% of the added mass comes in the form of cloud water, while rain (25%) and graupel (19%) also make large contributions. In the outer region, cloud water makes up 60% of the added water mass, rain contributes 17%, and graupel and cloud ice account for 10-11%. The larger contribution from cloud ice in the outer region comes from its occurrence over a very widespread area.

This problem cannot be lessened by reducing the time step since, even though the resulting negative mixing ratios may become smaller, the correction is applied over a greater number of time steps. Increased grid resolution is also not likely to yield much improvement, since the error is related to advection across sharp gradients and these gradients are likely to be sharper as resolution is improved. The only reliable solution is to switch from the centered-leapfrog differencing to a positive-definite advection scheme. While the artificial source is nonphysical, it does not necessarily produce more mass than would occur if a positive-definite advection scheme were used. The leapfrog, centered differencing scheme is strongly damping of poorly resolved structures so that the artificial source effectively adds back some of the mass lost to damping while increasing dispersion in the upstream direction.

6. Conclusions

A detailed water budget is performed using a high-resolution simulation of Hurricane Bonnie (1998). The simulation generally reproduces the track, intensity, and structure of the storm, but overpredicts the precipitation as inferred from comparison of model and TRMM radar reflectivities. The water vapor budget confirms that the ocean source of vapor in the eyewall region is very small relative to the condensation and inward transport of vapor, with the ocean vapor source being approximately 4% of the inward vapor transport into the eyewall region. This result is in agreement with earlier observational and modeling studies by Malkus and Riehl (1960) and Kurihara (1975) and suggests that other observation-based studies (Hawkins and Rubsam 1968, Hawkins and Imbembo 1976, Gamache et al. 1993) generally overestimated the role of the ocean source by underestimating the radial transport of moisture in the lowest 500 m.

The cloud condensate budget shows that, for a mature storm, the azimuthally-averaged cloud amount is consumed about as fast as it is produced. Cloud liquid water often peaks within

the melting layer as cooling by melting enhances condensation in this layer. This liquid water is lofted above the melting layer in the updrafts and is subsequently collected by precipitating hydrometeors. In the eyewall, most of the condensation occurs within convective towers while in the outer regions, condensation is dominated by stratiform precipitation processes.

Precipitation is dominated by production and fallout with little precipitation mass from the eyewall being transported radially outward into the surrounding stratiform rain area. Much of the mass that is transported outward is in the form of smaller ice particles at upper-most levels that provide seeds for additional particle growth by deposition and aggregation. Similar to Gamache et al. (1993), an asymmetric pattern of outflow caused by environmental vertical wind shear leads to an asymmetric pattern of hydrometeor seeding with much of the detrained ice mass exiting the eyewall on the southeast (rear and downshear) side of the storm.

To derive a complete condensed water budget, an artificial source of water must be included that is associated with setting negative mixing ratios to zero. These negative values arise because of numerical advection errors associated with the centered-in-space, leapfrog time differencing. Most of this added water mass comes in the form of cloud liquid water, although rain, graupel, and to a lesser extent cloud ice also make significant contributions. For the cloud fields, this source is rather weak in magnitude but very widespread, whereas for the precipitation categories, the source is concentrated along the inner edge of the eyewall and within the melting layer.

While not the goal of this study, some conclusions may be drawn from the budget results regarding the overprediction of higher reflectivities in the model compared to those observed by TRMM. Such a problem may result from the cloud microphysical scheme, but if the higher simulated reflectivities actually represent an overproduction of precipitation mass rather than errors in the specified particle size distributions, then it is probable that no amount of tuning or improvement of the microphysics will alleviate the problem. Instead, the problem may lie with the net production of water mass, which is approximately equal to the net radial import of moisture in the boundary layer. This problem, in turn, may result from either a positive bias in the boundary layer temperature and vapor mixing ratio or in the intensity of the radial inflow. Consequently, the overproduction of precipitation may be the result of the boundary layer parameterization and not the cloud microphysics parameterization. This topic requires further attention in future research.

Acknowledgements: The author gratefully acknowledges Dr. Zhaoxia Pu for providing the initial conditions for the simulation. This work was supported by Dr. Ramesh Kakar at NASA Headquarters with funds from the NASA CAMEX-4 and Precipitation Science programs.

References

Braun, S. A., 2002: A cloud-resolving simulation of Hurricane Bob (1991): Storm structure and eyewall buoyancy. *Mon. Wea. Rev.*, **130**, 1573-1592.

———, and W.-K. Tao, 2000: Sensitivity of high-resolution simulations of Hurricane Bob (1991) to planetary boundary layer parameterizations. *Mon. Wea. Rev.*, **128**, 3941-3961.

———, M. T. Montgomery, and Z. Pu, 2004: The Organization of vertical motion in as asymmetric Hurricane – Bonnie (1998). Submitted to *J. Atmos. Sci.*

Byers, H. R., 1944: *General meteorology*. New York, McGraw-Hill Book Co., 645 pp.

Churchill, D. D., and R. A. Houze, Jr., 1984: Mesoscale updraft magnitude and cloud-ice content deduced from the ice budget of a tropical cloud cluster. *J. Atmos. Sci.*, **41**, 1717-1725.

Dudhia, J, 1989: Numerical study of convection observed during the winter monsoon experiments using a mesoscale two-dimensional model. *J. Atmos. Sci.*, **46**, 3077-3107.

———, 1993: A nonhydrostatic version of the Penn State-NCAR mesoscale model: Validation tests and simulation of an Atlantic Cyclone and cold front. *Mon. Wea. Rev.*, **121**, 1493-1513.

Gamache, J. F., and R. A. Houze, Jr., 1983: Water budget of a mesoscale convective system in the tropics. *J. Atmos. Sci.*, **40**, 1835-1850.

———, ———, and F. D. Marks, Jr., 1993: Dual-aircraft investigation of the inner core of Hurricane Norbert. Part III: Water Budget. *J. Atmos. Sci.*, **50**, 3221-3243.

Garratt, J. R., 1992: *The Atmospheric Boundary Layer*, Cambridge University Press, 316 pp.

Grell, G. A., J. Dudhia, and D. R. Stauffer, 1995: A description of the fifth-generation Penn State/NCAR Mesoscale Model (MM5). NCAR Technical Note (NCAR/TN-398+STR), 122 pp.

Hawkins, H. F., and S. M. Imbembo, 1976: The structure of a small, intense hurricane—Inez 1966. *Mon. Wea. Rev.*, **104**, 418-442.

———, and D. T. Rusbam, 1968: Hurricane Hilda, 1964. II. Structure and budgets of the hurricane on October 1, 1964. *Mon. Wea. Rev.*, **96**, 617-636.

Jorgensen, D. P., E. J. Zipser, and M. A. LeMone, 1985: Vertical motions in intense hurricanes. *J. Atmos. Sci.*, **42**, 839-856.

Kurihara, Y., 1975: Budget analysis of a tropical cyclone simulated in an axisymmetric numerical model. *J. Atmos. Sci.*, **32**, 25-59.

Malkus, J., and H. Riehl, 1960: On the dynamics and energy transformations in steady-stte hurricanes. *Tellus*, **12**, 1-20.

Manning, K. W., and P. L. Haagenson, 1992: Data ingest and objective analysis for the PSU/NCAR modeling system: Programs DATAGRID and RAWINS. NCAR Technical Note (NCAR/TN-376+IA), 209 pp.

Marks, F., Jr., 1985: Evolution of the structure of precipitation in Hurricane Allen (1980). *Mon. Wea. Rev.*, **113**, 909-930.

———, and R. A. Houze, Jr., 1987: Inner core structure of Hurricane Alicia from airborne doppler radar observations. *J. Atmos. Sci.*, **44**, 1296-1317.

Mlawer, E. J., S. J. Taubman, P. D. Brown, M. J. Iacono, and S. A. Clough, 1997: Radiative transfer for inhomogeneous atmosphere: RRTM, a validated correlated-k model for the longwave. *J. Geophys. Res.*, **102 (D14)**, 16663-16682.

Ooyama, K., 1969: Numerical simulation of the life cycle of tropical cyclones. *J. Atmos. Sci.*, **26**, 3-40.

Pagowski, M., and G. W. K. Moore, 2001: A numerical study of an extreme cold-air outbreak over the Labrador Sea: Sea Ice, air-sea interaction, and development of polar lows. *Mon. Wea. Rev.*, **129**, 47-72.

Palmen, E., and H. Riehl, 1957: Budget of angular momentum and energy in tropical cyclones. *J. Meteor.*, **14**, 150-159.

Pu, Z., and S. Braun, 2001: Evaluation of bogus vortex techniques with four-dimensional variational data assimilation. *Mon. Wea. Rev.*, **129**, 2023-2039.

Riehl, H., 1954: *Tropical meteorology*. New York, McGraw-Hill Book Co., 392 pp.

Riehl, H., and J. S. Malkus, 1961: Some aspects of Hurricane Daisy, 1958. *Tellus*, **13**, 181-213.

Rogers, R, S. Chen, J. Tenerelli, and H. Willoughby, 2003: A numerical study of the impact of vertical shear on the distribution of rainfall in Hurricane Bonnie (1998), *Mon. Wea. Rev.*, **131**, 1577-1599.

Smull, B. F., and R. A. Houze, Jr., 1985: A midlatitude squall line with a trailing region of stratiform rain: Radar and satellite observations. *Mon. Wea. Rev.*, **113**, 117-133.

Xiao, Q, X. Zou, and B. Wang, 2000: Initialization and simulation of a landfalling hurricane using variational bogus data assimilation scheme. *Mon. Wea. Rev.*, **187**, 2252-2269.

Yuter, S. E., and R. A. Houze, Jr., 1995: Three-dimensional kinematic and microphysical evolution of Florida cumulonimbus. Part III: Vertical mass transport, mass divergence, and synthesis. *Mon. Wea. Rev.*, **123**, 1964-1983.

Zhang, D.-L., Y. Liu, and M. K. Yau, 2002: A multiscale numerical study of Hurricane Andrew (1992). Part V.: Inner-core thermodynamics. *Mon. Wea. Rev.*, **130**, 2745-2763.

Zhu, T., D.-L. Zhang, and F. Weng, 2003: Numerical simulation of hurricane Bonnie (1998). Part I: Eyewall evolution and intensity changes. *Mon. Wea. Rev.*, (submitted).

Zou, X., and Q. Xiao, 2000: Studies on the initialization and simulation of a mature hurricane using a variational bogus data assimilation scheme. *J. Atmos. Sci.*, **57**, 836-860.

Figure Captions

Figure 1. TRMM radar reflectivity at 2 km MSL at (a) 1800 UTC 22 August and (b) 1050 UTC 24 August 1998. (c) Simulated radar reflectivity at 2 km MSL valid 1200 UTC 23 August.

Figure 2. Contoured frequency by altitude diagrams of (a) TRMM radar reflectivity at 1800 UTC 22 August and (b) MM5 simulated reflectivity at 1200 UTC 23 August 1998. Contours of frequency are drawn at 0.01, 1, 2.5, 5, 7.5, 10% and intervals of 5% thereafter. Shading is as follows: light shading, 1-5%; medium shading, 5-10%; and dark shading, 10-20%.

Figure 3. Shading indicates simulated radar reflectivity at (a) 40 m, (b) 2.7 km, (c) 6.8 km, and (d) 12.0 km, with contours drawn at 15, 25, 35, and 45 dBZ (light, medium, dark, and no shading, respectively). Contour overlays are (a, d) storm-relative radial velocity and (b, c) vertical velocity. Contours in (a, d) are drawn at 5 m s^{-1} intervals and in (b, c) at 0.25 m s^{-1} for $w<0$ and 0.5 m s^{-1} for $w>0$. Solid (dashed) lines indicate positive (negative) values, with the 0 and 20 m s^{-1} contours in (a) and (d) highlighted. Vertical velocities have been smoothed to improve clarity. The straight solid line in (c) indicates the position of the vertical cross sections in Fig. 4.

Figure 4. Shading indicates simulated radar reflectivity in (a, c) and total cloud mixing ratio in (b) at Y=0 km (see Fig. 3). Shaded contours are drawn at 10, 20, 30, and 40 dBZ (light, medium, dark, and no shading, respectively) in (a, c) and at 0.1, 0.2, 0.4, 0.6, and 0.8 g kg^{-1} (light, medium, medium-dark, dark, and light) in (b). Contour overlays are (a, b) vertical velocity and (c) storm-relative radial velocity. Contours in (a, b) are drawn at 0.5 m s^{-1} for $w<0$ and 1 m s^{-1} for $w>0$ with an additional contour at 0.5 m s^{-1}, and in (c) 5 m s^{-1} intervals. Solid (dashed) lines indicate positive (negative) values.

Figure 5. Azimuthally averaged fields for (a) tangential velocity, 5 m s^{-1} intervals; (b) radial velocity, 3 m s^{-1} intervals for $u<0$ and 2 m s^{-1} for $u>0$; (c) vertical velocity, 0.2 m s^{-1} intervals for $w>0$ and 0.1 m s^{-1} for $w<0$; (d) water vapor mixing ratio departure from domain averaged value, 0.3 g kg^{-1} intervals; (e) cloud water and ice mixing ratios, 0.1 g kg^{-1} intervals with an extra contour at 0.01 g kg^{-1} and shading indicating cloud liquid water >0.01 g kg^{-1}; and (f) rain

(shading), snow (thin contours), and graupel (thick contours). Contours are drawn at 0.3 g kg^{-1} intervals with an extra contour at 0.01 g kg^{-1}. Light shading in upper half of panel indicates areas of radial outflow. Solid (dashed) lines indicate positive (negative) values.

Figure 6. Water vapor budget fields showing (a) condensation, (b) horizontal flux divergence, (c) evaporation, (d) vertical flux divergence, (e) net condensation (sum of a and c), (f) total advection (sum of b and d), (g) divergence term, and (h) boundary layer source term. Contour intervals in (a, e, and f) are 2 g kg^{-1} h^{-1}, with an extra contour at 1 g kg^{-1} h^{-1}. Contour values in (b) and (d) are at 20 g kg^{-1} h^{-1} intervals, with and extra contour at 10 g kg^{-1} h^{-1}. Contour values in (c, g and h) are at 0.5 g kg^{-1} h^{-1} intervals. In (b, d, and h), only the lowest 5 km are shown to improve readability since values above these levels are negligible. Solid (dotted) lines indicate positive (negative) values.

Figure 7. Shading indicates the cumulative percentage of the area occupied by updrafts less than the indicated value. Contours are drawn at 10% intervals, with additional contours at 95 and 99%. Thick lines show the cumulative percentage of total condensation occurring in updrafts less than the indicated values. (a) Eyewall region, (b) outer region.

Figure 8. Azimuthally averaged cloud budget fields showing (a) cloud sink, (b) horizontal flux divergence, (c) net source, (d) vertical flux divergence, (e) boundary layer source, and (f) added water mass to offset negative mixing ratios. The contour interval in (a) is 2 g kg^{-1} h^{-1}, with an extra contour at 1 g kg^{-1} h^{-1}. Contour values in (b-e) are at 0.5 g kg^{-1} h^{-1} intervals, with and extra contour at 0.25 g kg^{-1} h^{-1}. Contour values in (f) are at 0.125 and 0.25 g kg^{-1} h^{-1}. In (e), only the lowest 5 km are shown to improve readability since values above these levels are negligible. Solid (dotted) lines indicate positive (negative) values.

Figure 9.Azimuthally averaged precipitation source terms showing sources (a, c, and e) and sinks (b, d, and f) for rain, graupel, and snow, respectively. The contour interval is 2 g kg^{-1} h^{-1}, with an extra contour at 1 g kg^{-1} h^{-1}. Solid (dotted) lines indicate positive (negative) values.

Figure 10. Azimuthally averaged precipitation budget fields showing the (a) net microphysical source, (b) horizontal flux divergence, (c) precipitation fallout and vertical flux divergence, and (d) added water mass to offset negative mixing ratios. The contour interval in (a-c) is 2 g kg^{-1} h^{-1}, with an extra contour at 1 g kg^{-1} h^{-1}. Contour values in (d) are at 0.5 g kg^{-1} h^{-1} intervals. Solid (dotted) lines indicate positive (negative) values.

Figure 11. Vertically integrated source terms for (a) condensation, (b) evaporation, and (c) precipitation fallout. Contour intervals in (a, c) are 2 g kg^{-1} h^{-1} with additional contours at 1 g kg^{-1} h^{-1} (light and medium shading at 0.2 and 0.6 g kg^{-1} h^{-1}) The contour interval in (b) is 0.5 g kg^{-1} h^{-1} (light, medium and dark shading at 0.5, 1.0, and 1.5 g kg^{-1} h^{-1}).

Figure 12. Vertically integrated source terms for (a) total rain source, (b) warm-rain source (rain source plus graupel sink), (c) cold-rain source (graupel sink), and (d) graupel source. Contour intervals are 1 g kg^{-1} h^{-1} with light, medium and dark shading at 1, 4, and 8 g kg^{-1} h^{-1}.

Figure 13. (a) Water vapor budget and (b) total condensate (cloud plus precipitation) budget. The left portion of the diagrams represent the inner-core area (eye and eyewall, r<70 km) while the right portion is for the outer region (70 km< r< 200 km). Parameter names are provided in Table 1. All values are normalized by the total condensation in r < 200 km.

Figure 14. Azimuthally averaged mixing ratios and source terms associated with setting negative mixing ratios to zero for (a) cloud liquid water, (b) cloud ice, (c) rain, (d) graupel, and (e) snow. Shaded contours of cloud water in (a) are drawn at 0.1 g kg^{-1} intervals, with an extra contour at 0.01 g kg^{-1}. For the remaining hydrometeors (shading, b-e), the contour interval is 0.5 g kg^{-1}, with an extra contour at 0.01 g kg^{-1}. Source terms (thick solid lines) are drawn at 0.5 g kg^{-1} h^{-1} intervals. For cloud ice and snow, extra contours (thin solid lines) are drawn at 0.125 g kg^{-1} h^{-1} intervals.

Figure 15. Vertically integrated source terms associated with setting negative mixing ratios to zero for (a) cloud water, (b) rain, and (c) graupel. Contours are drawn at 0.1 g kg^{-1} h^{-1} intervals with light, medium, and dark shading at 0.1, 0.3, and 0.6 g kg^{-1} h^{-1}.

Table 1. Water budget parameter names, as shown in Figure 13.

Name	Term	Description/comment
Cond	$\overline{\overline{C}}$	Condensation+Deposition
Evap	$\overline{\overline{E}}$	Evaporation+Sublimation
VF	$\overline{\overline{-\frac{\partial(\rho_0 q_x w)}{\partial z}}}$	Vertical flux, typically negligible since w~0 at σ_s and σ_t
HAP	$\overline{\overline{-\nabla\cdot(\rho_0 q_x V')}} > 0$	Inward directed horizontal flux
HAM	$\overline{\overline{-\nabla\cdot(\rho_0 q_x V')}} < 0$	Outward directed horizontal flux
Div	$\overline{\overline{\rho_0 q_x\left(\nabla\cdot V' + \frac{\partial w}{\partial z}\right)}}$	Divergence term
P	$\overline{\overline{\frac{\partial(\rho_0 q_p V_T)}{\partial z}}}$	Surface precipitation flux
Diff	$\overline{\overline{\rho_0 D_x}}$	Numerical diffusion
PBL	$\overline{\overline{\rho_0 B_x}}$	Boundary layer source
Zero	$\overline{\overline{\rho_0 Z_x}}$	Mass added to offset spurious negative mixing ratios
Tend	$\overline{\overline{\frac{\partial(\rho_0 q_x)}{\partial t}}}$	Storage term

Table 2. Breakdown of the Zero term in the condensed water budget in Fig. 13b for each hydrometeor category. Numbers show the amount, normalized by the total condensation, and the percent contribution to the total in parentheses.

Mixing Ratio Field	Eyewall region (r< 70 km)	Outer region (70<r<200 km)
Cloud liquid water (q_c)	1.02 (41%)	6.18 (60%)
Cloud ice (q_i)	0.28 (11%)	1.13 (11%)
Rain (q_r)	0.61 (25%)	1.74 (17%)
Graupel (q_g)	0.46 (19%)	1.04 (10%)
Snow (q_s)	0.09 (4%)	0.28 (3%)

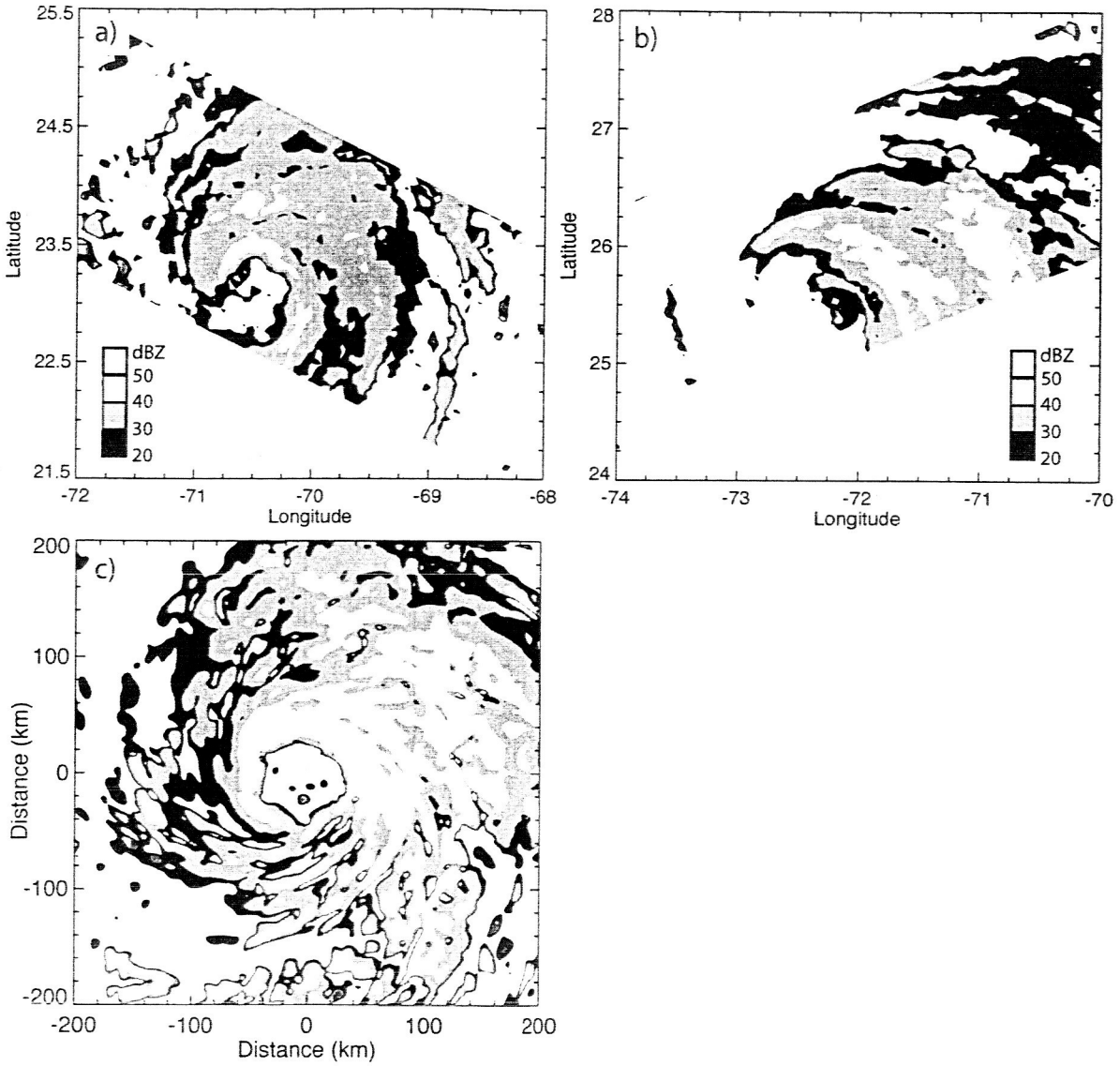

Figure 1. TRMM radar reflectivity at 2 km MSL at (a) 1800 UTC 22 August and (b) 1050 UTC 24 August 1998. (c) Simulated radar reflectivity at 2 km MSL valid 1200 UTC 23 August.

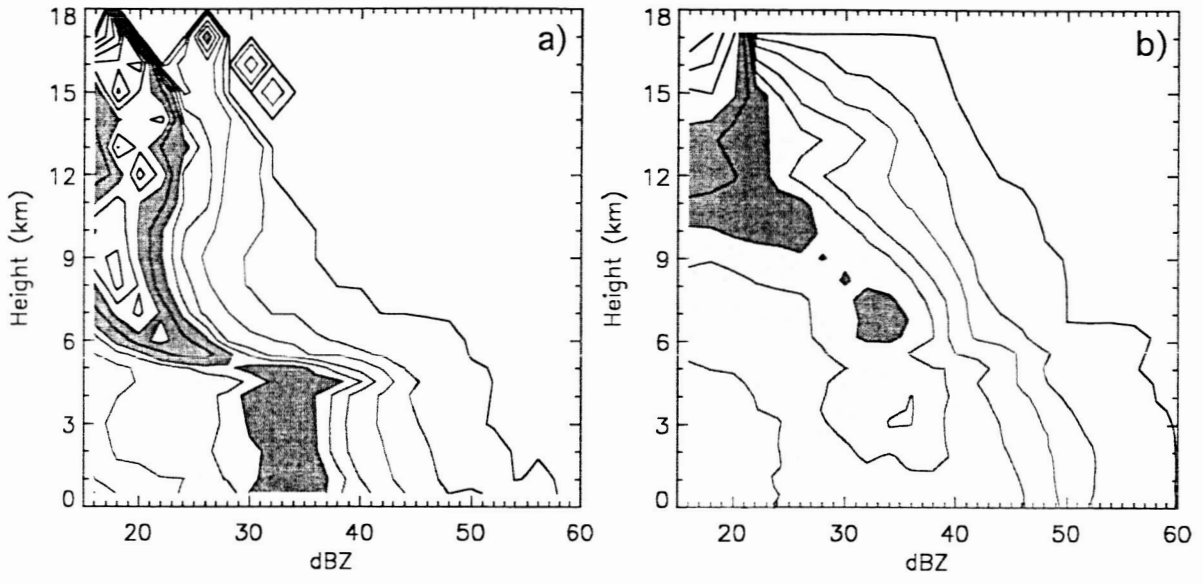

Figure 2. Contoured frequency by altitude diagrams of (a) TRMM radar reflectivity at 1800 UTC 22 August and (b) MM5 simulated reflectivity at 1200 UTC 23 August 1998. Contours of frequency are drawn at 0.01, 1, 2.5, 5, 7.5, 10% and intervals of 5% thereafter. Shading is as follows: light shading, 1-5%; medium shading, 5-10%; and dark shading, 10-20%.

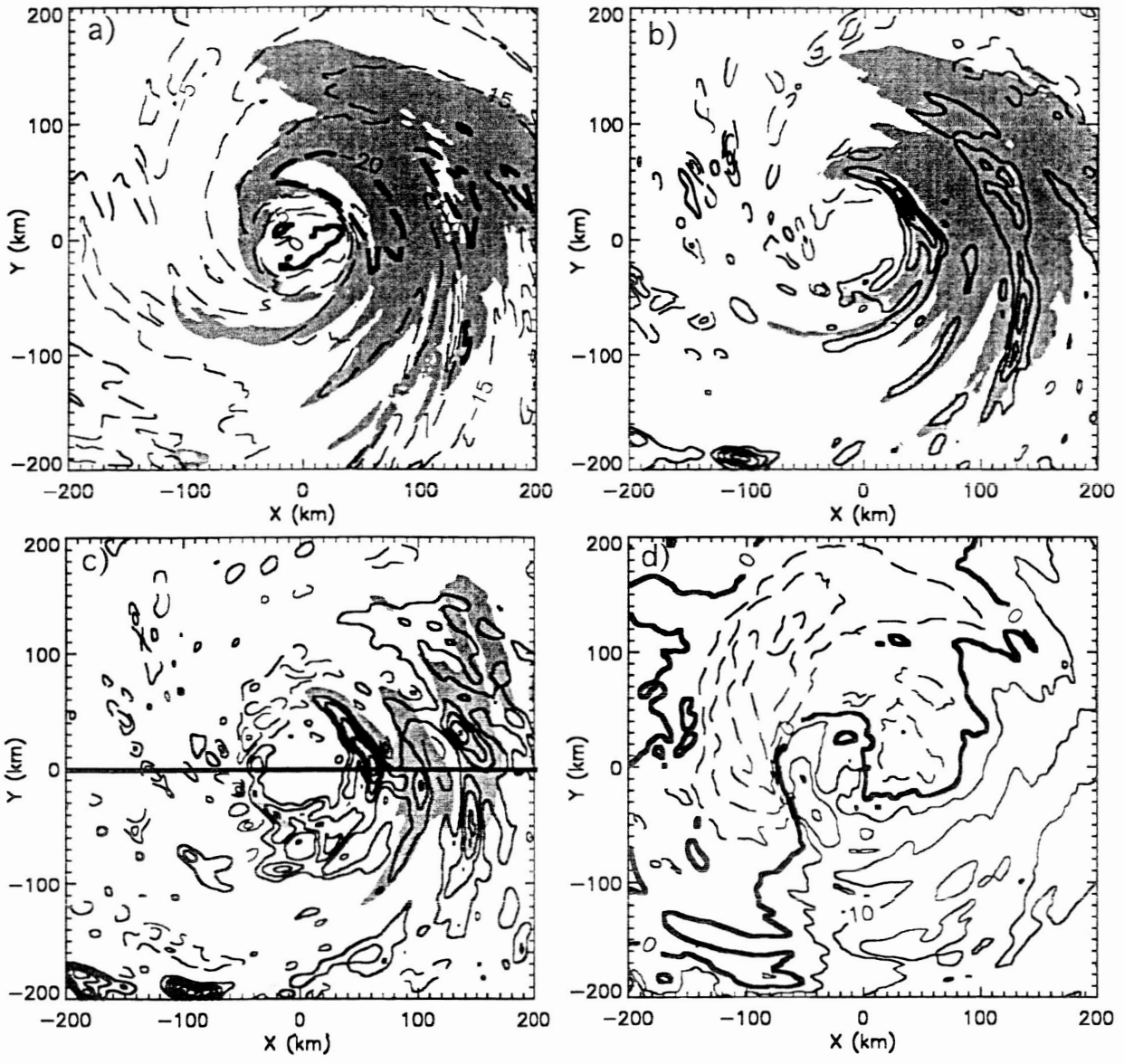

Figure 3. Shading indicates simulated radar reflectivity at (a) 40 m, (b) 2.7 km, (c) 6.8 km, and (d) 12.0 km, with contours drawn at 15, 25, 35, and 45 dBZ (light, medium, dark, and no shading, respectively). Contour overlays are (a, d) storm-relative radial velocity and (b, c) vertical velocity. Contours in (a, d) are drawn at 5 m s^{-1} intervals and in (b, c) at 0.25 m s^{-1} for $w<0$ and 0.5 m s^{-1} for $w>0$. Solid (dashed) lines indicate positive (negative) values, with the 0 and 20 m s^{-1} contours in (a) and (d) highlighted. Vertical velocities have been smoothed to improve clarity. The straight solid line in (c) indicates the position of the vertical cross sections in Fig. 4.

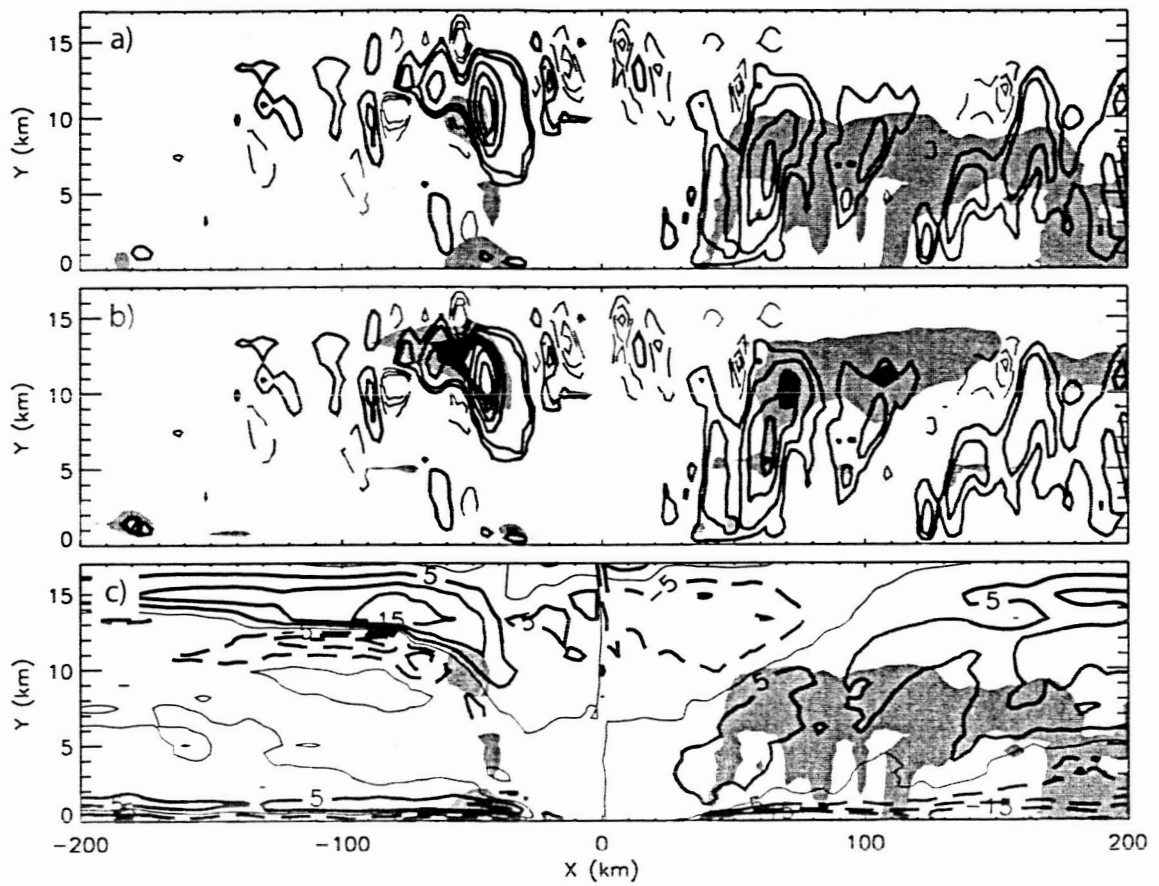

Figure 4. Shading indicates simulated radar reflectivity in (a, c) and total cloud mixing ratio in (b) at Y=0 km (see Fig. 3). Shaded contours are drawn at 10, 20, 30, and 40 dBZ (light, medium, dark, and no shading, respectively) in (a, c) and at 0.1, 0.2, 0.4, 0.6, and 0.8 g kg^{-1} (light, medium, medium-dark, dark, and light) in (b). Contour overlays are (a, b) vertical velocity and (c) storm-relative radial velocity. Contours in (a, b) are drawn at 0.5 m s^{-1} for w<0 and 1 m s^{-1} for w>0 with an additional contour at 0.5 m s^{-1}, and in (c) 5 m s^{-1} intervals. Solid (dashed) lines indicate positive (negative) values.

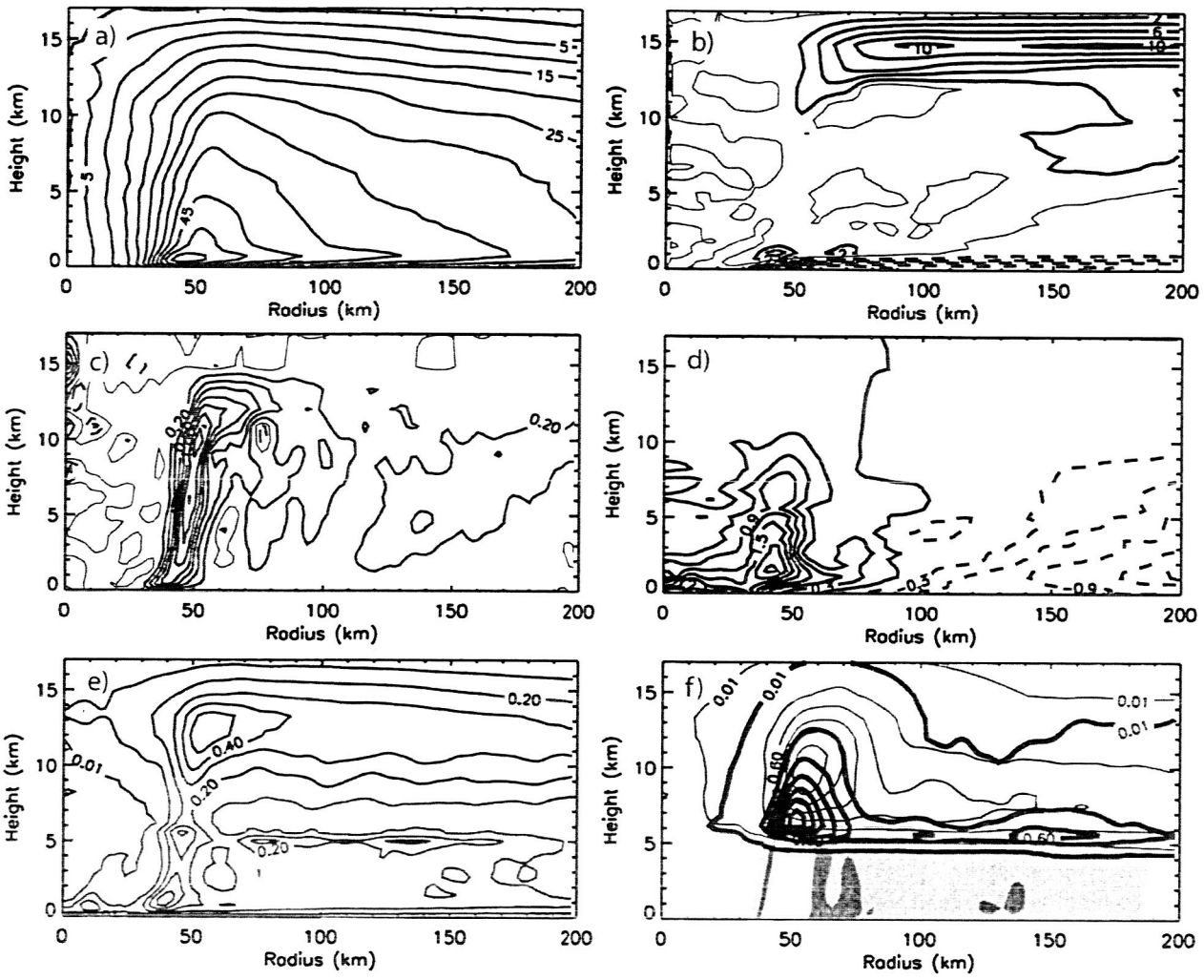

Figure 5. Azimuthally averaged fields for (a) tangential velocity, 5 m s^{-1} intervals; (b) radial velocity, 3 m s^{-1} intervals for $u<0$ and 2 m s^{-1} for $u>0$; (c) vertical velocity, 0.2 m s^{-1} intervals for $w>0$ and 0.1 m s^{-1} for $w<0$; (d) water vapor mixing ratio departure from domain averaged value, 0.3 g kg^{-1} intervals; (e) cloud water and ice mixing ratios, 0.1 g kg^{-1} intervals with an extra contour at 0.01 g kg^{-1} and shading indicating cloud liquid water >0.01 g kg^{-1}; and (f) rain (shading), snow (thin contours), and graupel (thick contours). Contours are drawn at 0.3 g kg^{-1} intervals with an extra contour at 0.01 g kg^{-1}. Light shading in upper half of panel indicates areas of radial outflow. Solid (dashed) lines indicate positive (negative) values.

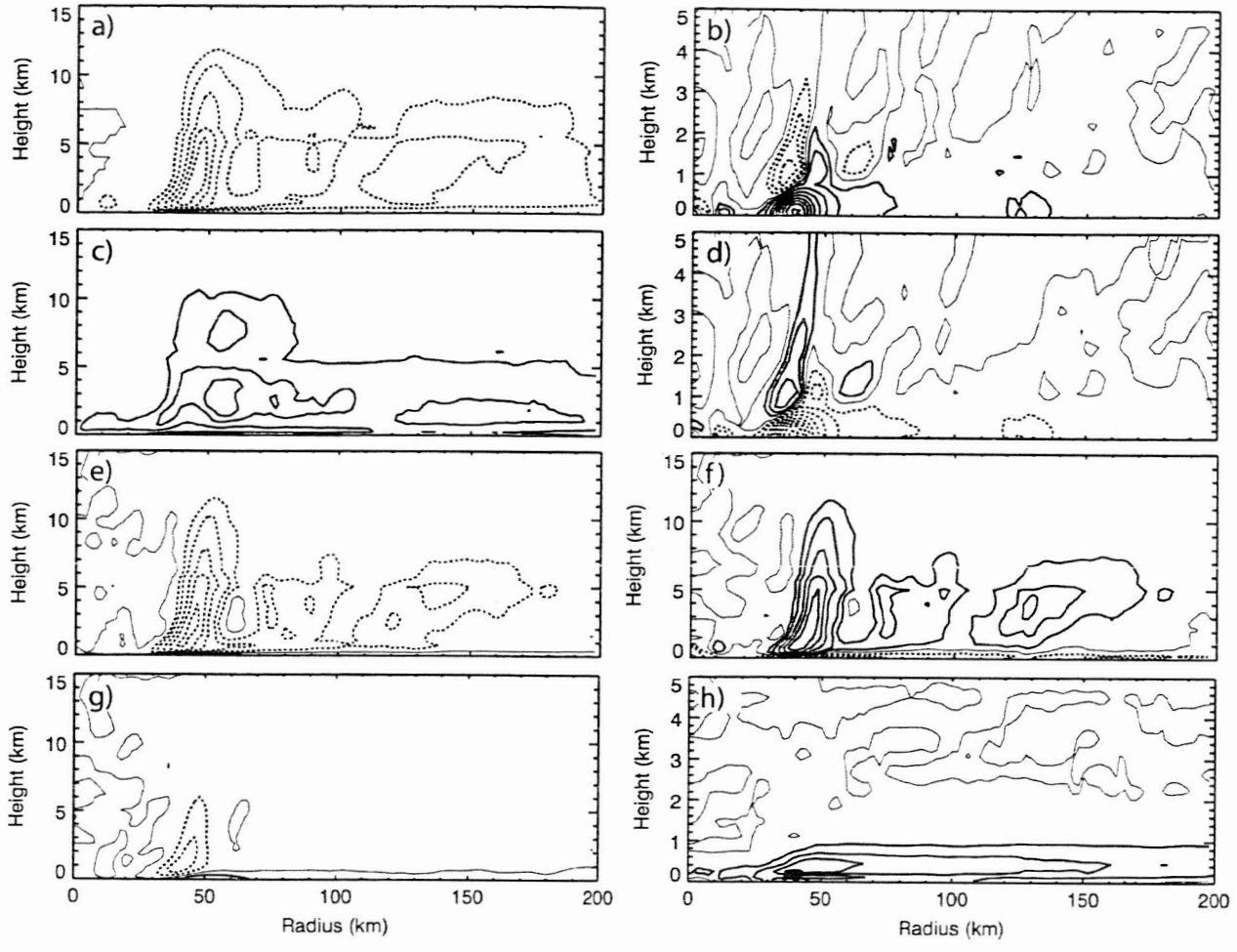

Figure 6. Water vapor budget fields showing (a) condensation, (b) horizontal flux divergence, (c) evaporation, (d) vertical flux divergence, (e) net condensation (sum of a and c), (f) total advection (sum of b and d), (g) divergence term, and (h) boundary layer source term. Contour intervals in (a, e, and f) are 2 g kg^{-1} h^{-1}, with an extra contour at 1 g kg^{-1} h^{-1}. Contour values in (b) and (d) are at 20 g kg^{-1} h^{-1} intervals, with and extra contour at 10 g kg^{-1} h^{-1}. Contour values in (c, g and h) are at 0.5 g kg^{-1} h^{-1} intervals. In (b, d, and h), only the lowest 5 km are shown to improve readability since values above these levels are negligible. Solid (dotted) lines indicate positive (negative) values.

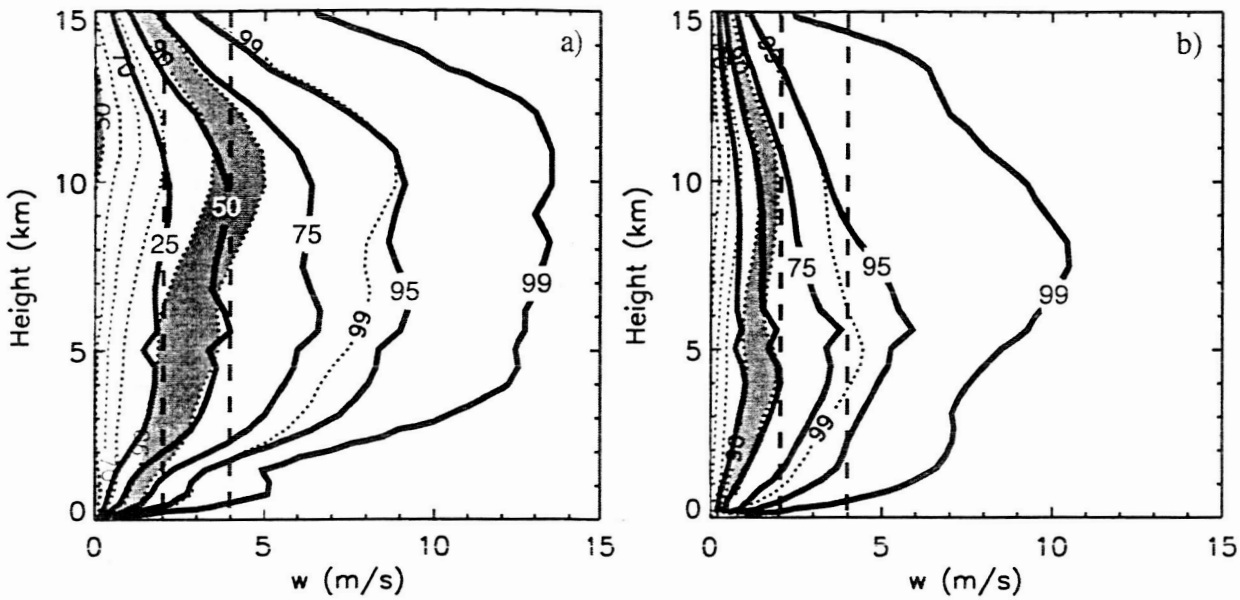

Figure 7. Shading indicates the cumulative percentage of the area occupied by updrafts less than the indicated value. Contours are drawn at 10% intervals, with additional contours at 95 and 99%. Thick lines show the cumulative percentage of total condensation occurring in updrafts less than the indicated values. (a) Eyewall region, (b) outer region.

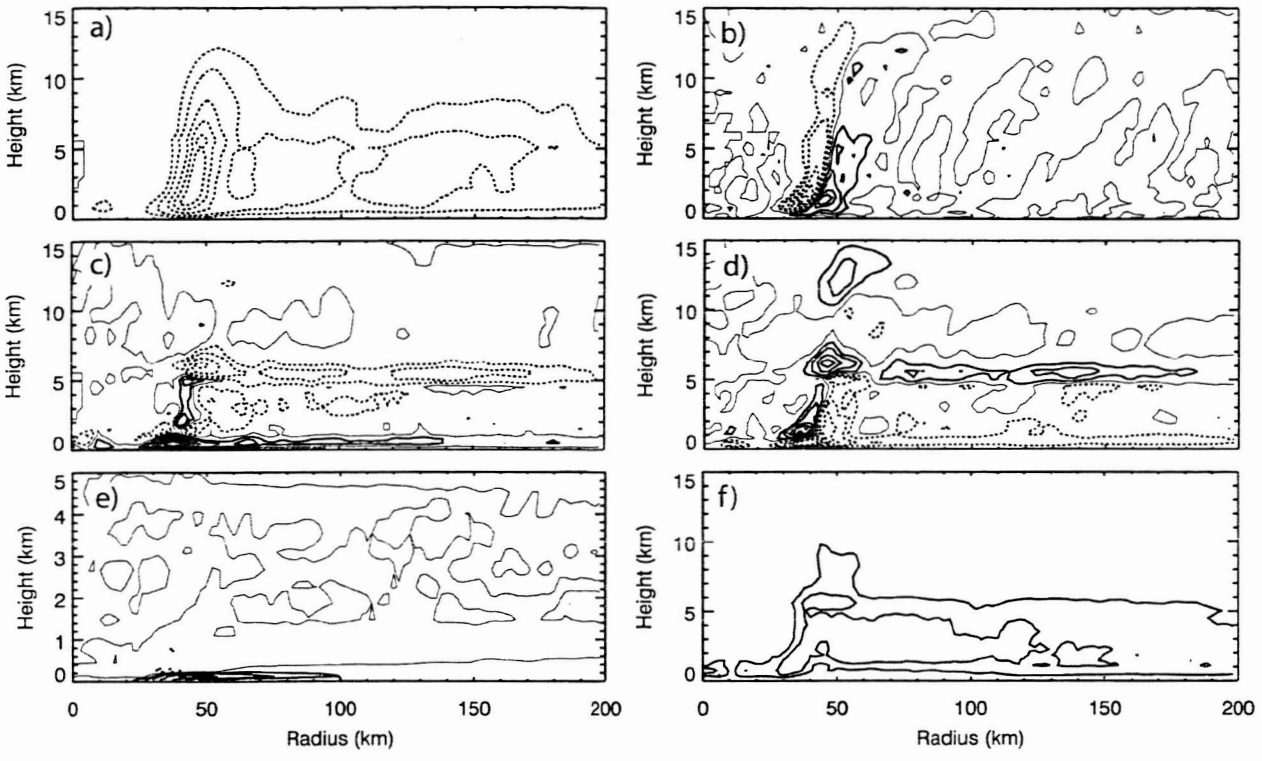

Figure 8. Azimuthally averaged cloud budget fields showing (a) cloud sink, (b) horizontal flux divergence, (c) net source, (d) vertical flux divergence, (e) boundary layer source, and (f) added water mass to offset negative mixing ratios. The contour interval in (a) is 2 g kg^{-1} h^{-1}, with an extra contour at 1 g kg^{-1} h^{-1}. Contour values in (b-e) are at 0.5 g kg^{-1} h^{-1} intervals, with and extra contour at 0.25 g kg^{-1} h^{-1}. Contour values in (f) are at 0.125 and 0.25 g kg^{-1} h^{-1}. In (e), only the lowest 5 km are shown to improve readability since values above these levels are negligible. Solid (dotted) lines indicate positive (negative) values.

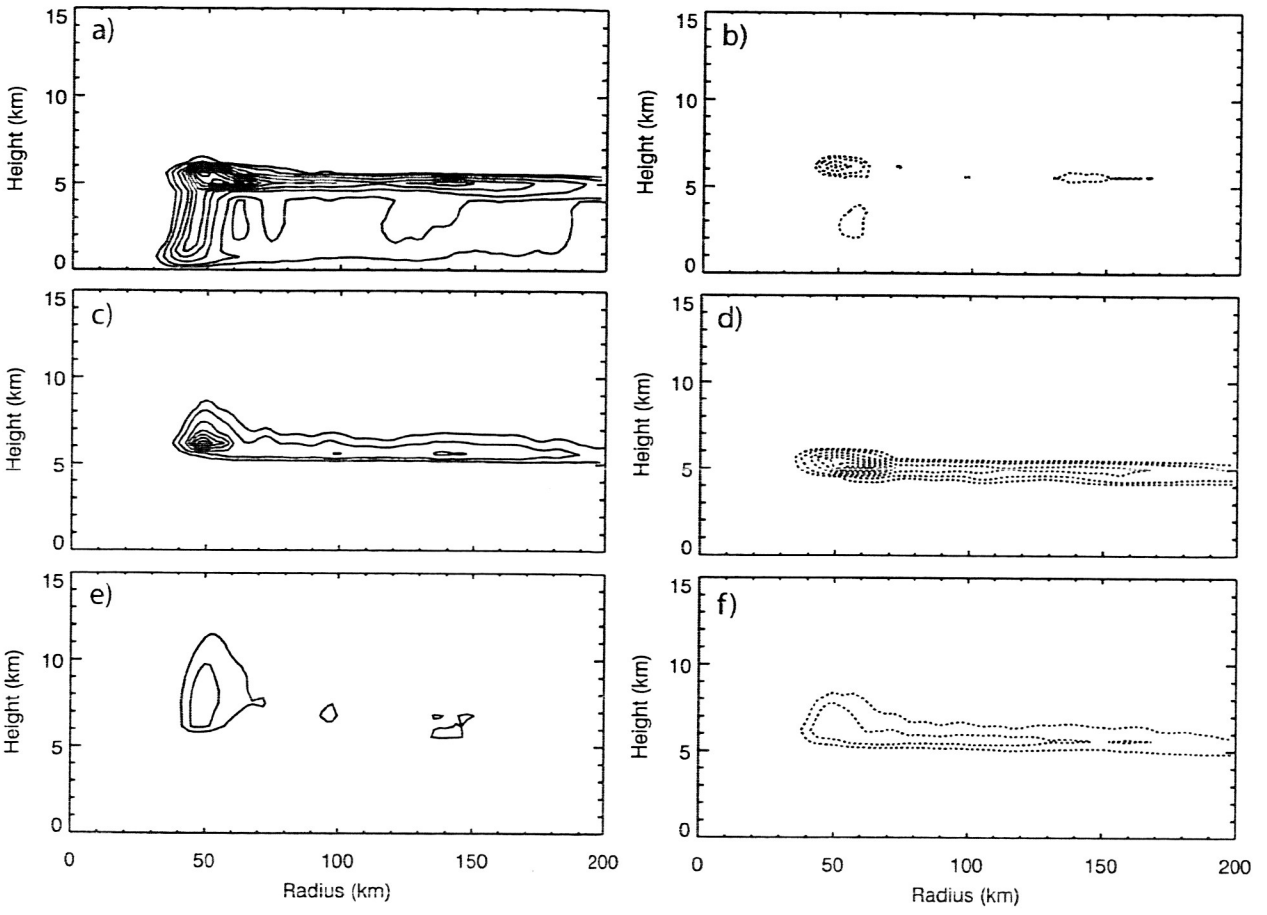

Figure 9.Azimuthally averaged precipitation source terms showing sources (a, c, and e) and sinks (b, d, and f) for rain, graupel, and snow, respectively. The contour interval is 2 g kg^{-1} h^{-1}, with an extra contour at 1 g kg^{-1} h^{-1}. Solid (dotted) lines indicate positive (negative) values.

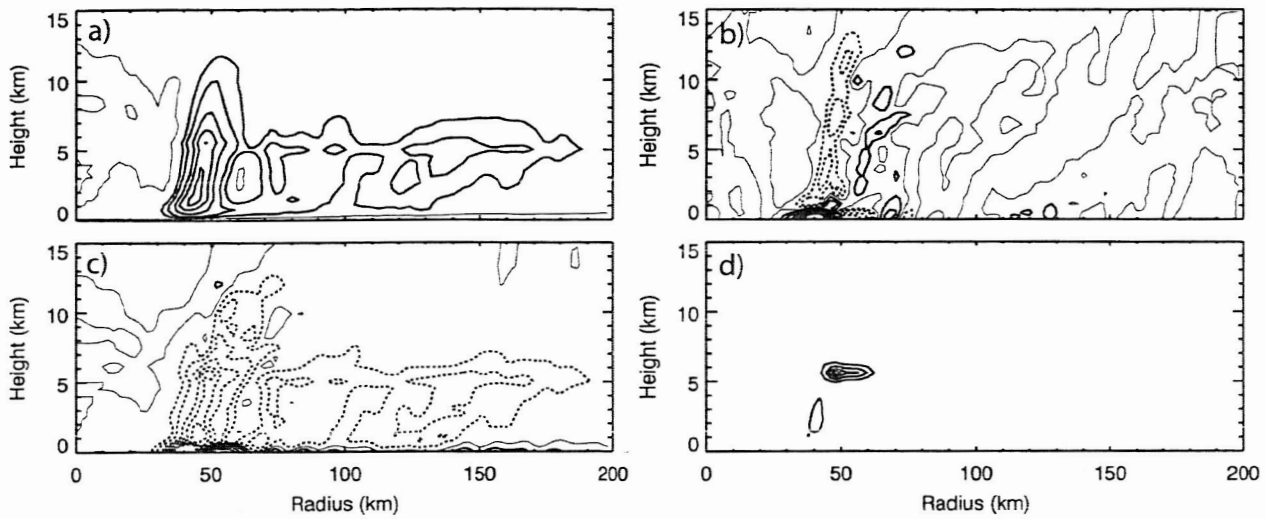

Figure 10. Azimuthally averaged precipitation budget fields showing the (a) net microphysical source, (b) horizontal flux divergence, (c) precipitation fallout and vertical flux divergence, and (d) added water mass to offset negative mixing ratios. The contour interval in (a-c) is 2 g kg^{-1} h^{-1}, with an extra contour at 1 g kg^{-1} h^{-1}. Contour values in (d) are at 0.5 g kg^{-1} h^{-1} intervals. Solid (dotted) lines indicate positive (negative) values.

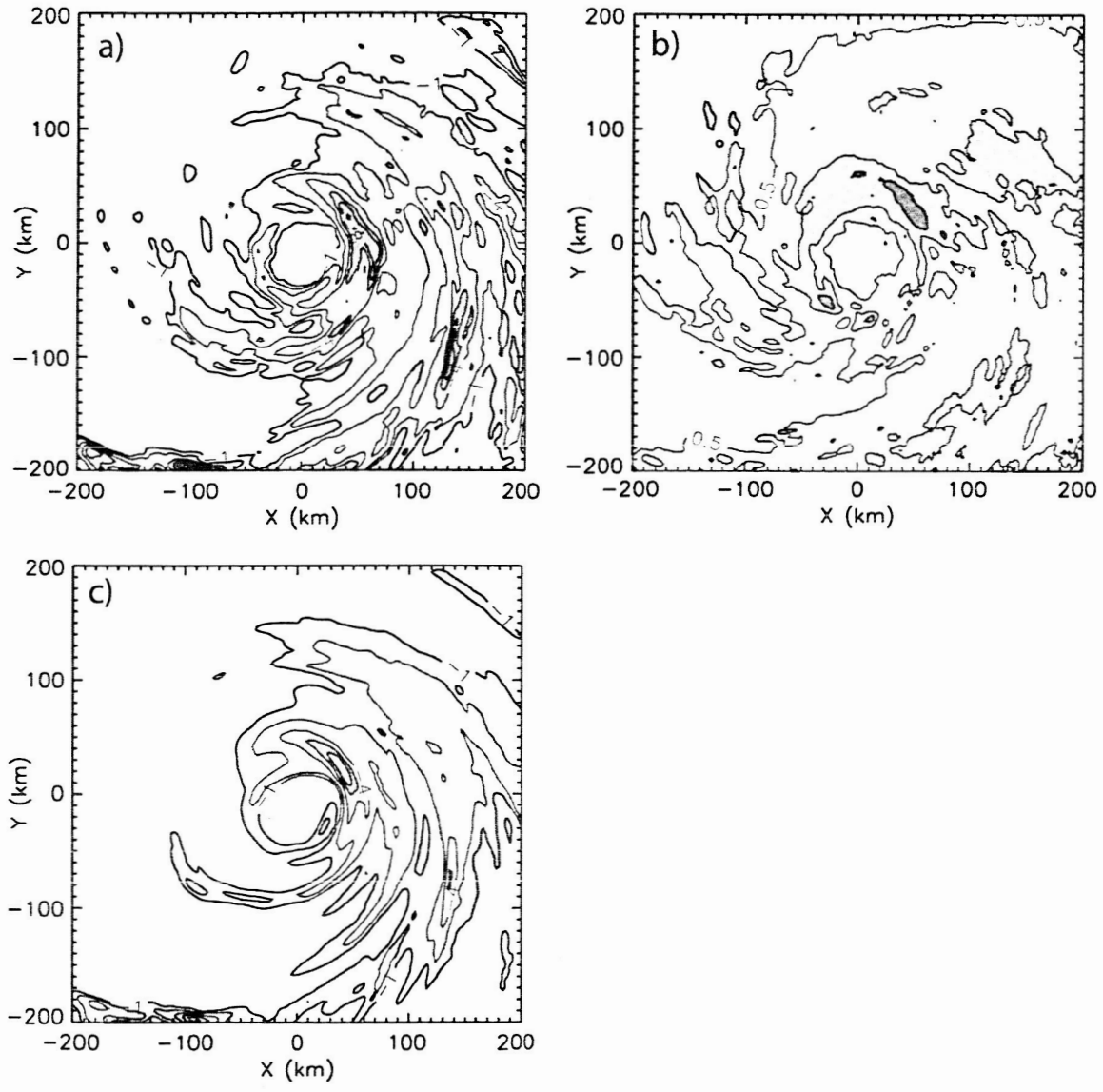

Figure 11. Vertically integrated source terms for (a) condensation, (b) evaporation, and (c) precipitation fallout. Contour intervals in (a, c) are 2 g kg^{-1} h^{-1} with additional contours at 1 g kg^{-1} h^{-1} (light and medium shading at 0.2 and 0.6 g kg^{-1} h^{-1}) The contour interval in (b) is 0.5 g kg^{-1} h^{-1} (light, medium and dark shading at 0.5, 1.0, and 1.5 g kg^{-1} h^{-1}).

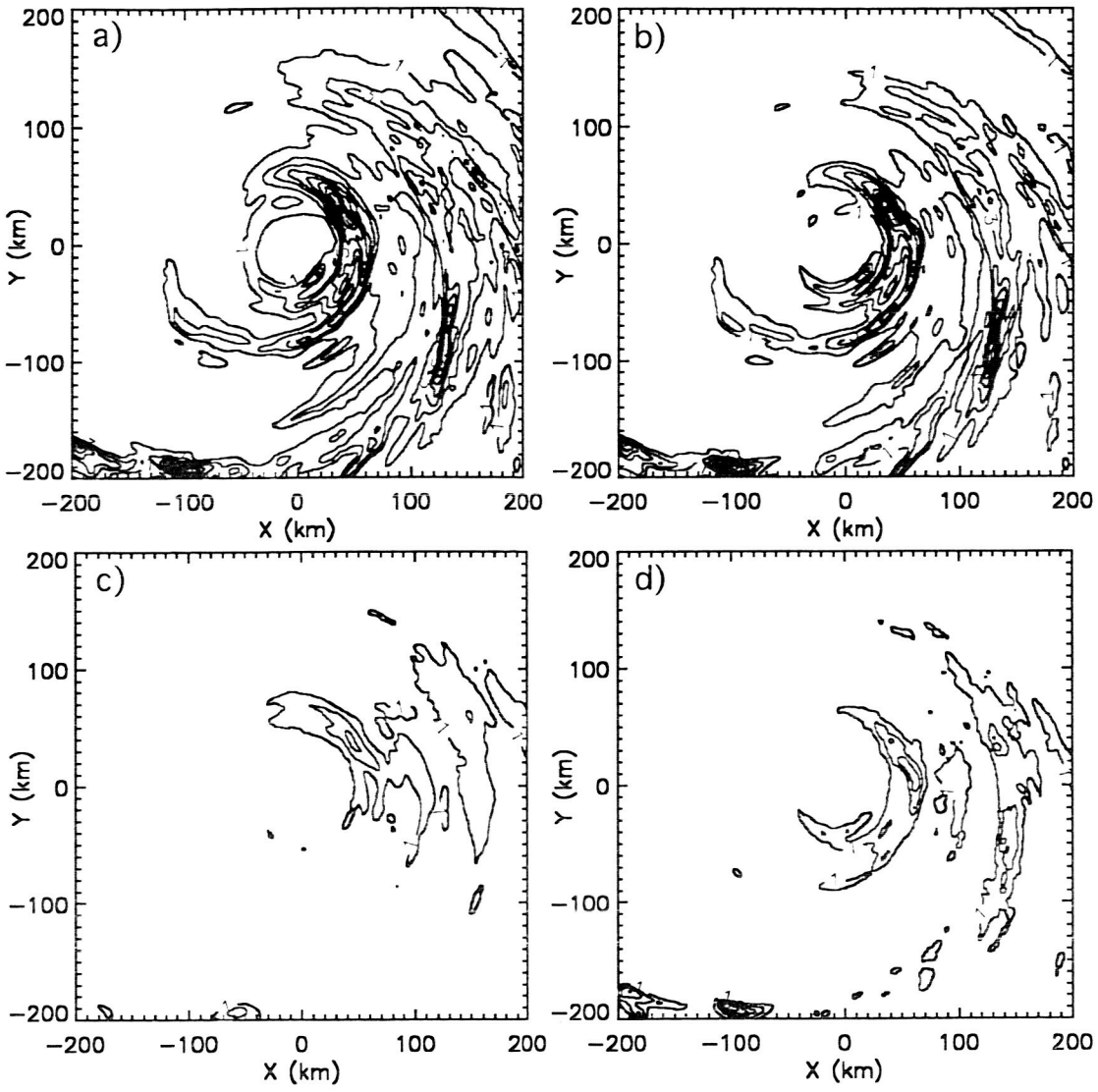

Figure 12. Vertically integrated source terms for (a) total rain source, (b) warm-rain source (rain source plus graupel sink), (c) cold-rain source (graupel sink), and (d) graupel source. Contour intervals are 1 g kg^{-1} h^{-1} with light, medium and dark shading at 1, 4, and 8 g kg^{-1} h^{-1}.

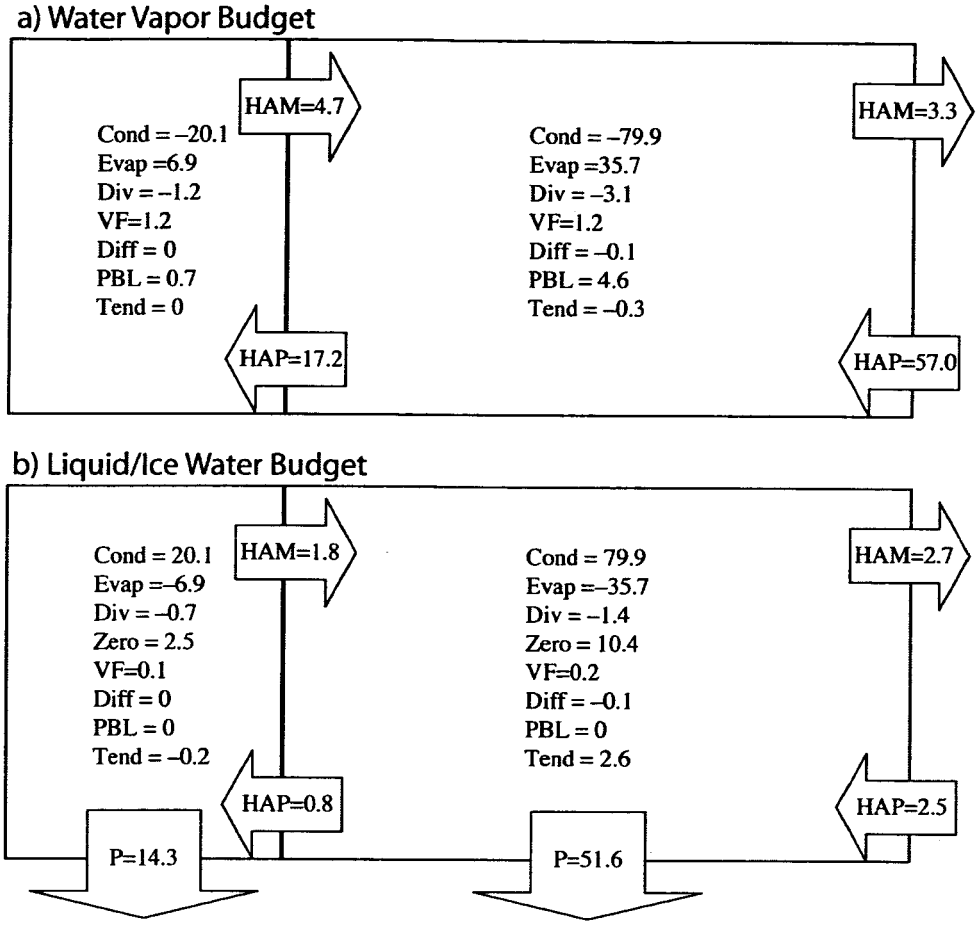

Figure 13. (a) Water vapor budget and (b) total condensate (cloud plus precipitation) budget. The left portion of the diagrams represent the inner-core area (eye and eyewall, r<70 km) while the right portion is for the outer region (70 km< r< 200 km). Parameter names are provided in Table 1. All values are normalized by the total condensation in r < 200 km.

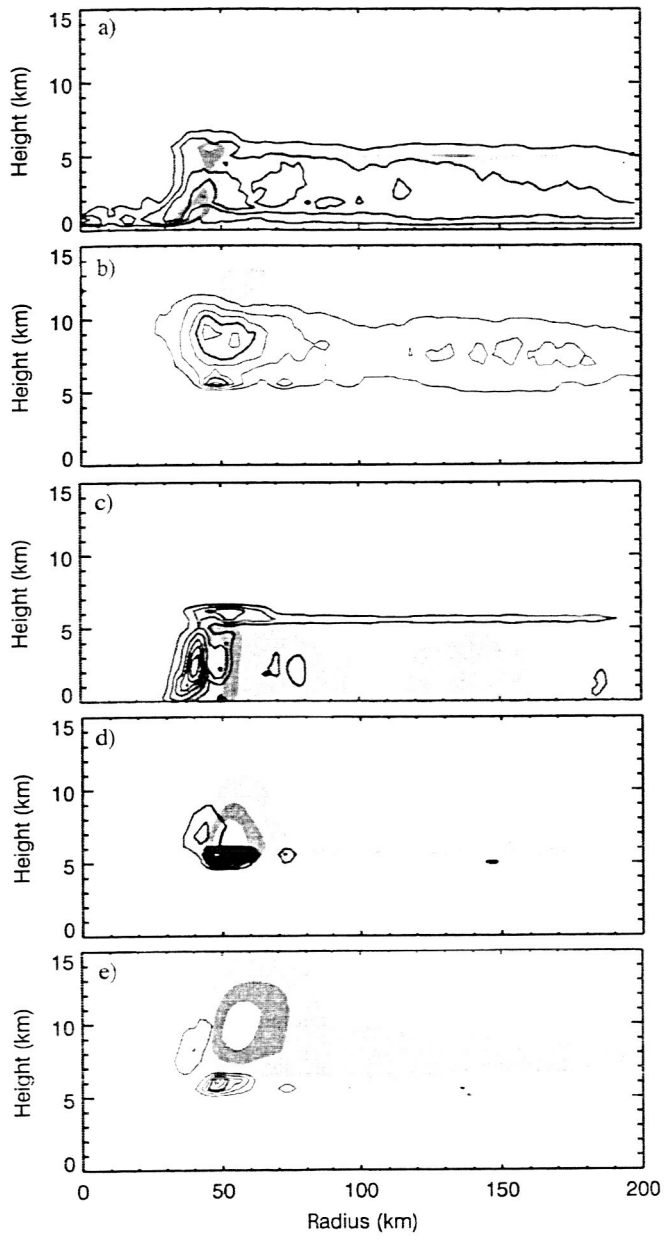

Figure 14. Azimuthally averaged mixing ratios and source terms associated with setting negative mixing ratios to zero for (a) cloud liquid water, (b) cloud ice, (c) rain, (d) graupel, and (e) snow. Shaded contours of cloud water in (a) are drawn at 0.1 g kg^{-1} intervals, with an extra contour at 0.01 g kg^{-1}. For the remaining hydrometeors (shading, b-e), the contour interval is 0.5 g kg^{-1}, with an extra contour at 0.01 g kg^{-1}. Source terms (thick solid lines) are drawn at 0.5 g kg^{-1} h^{-1} intervals. For cloud ice and snow, extra contours (thin solid lines) are drawn at 0.125 g kg^{-1} h^{-1} intervals.

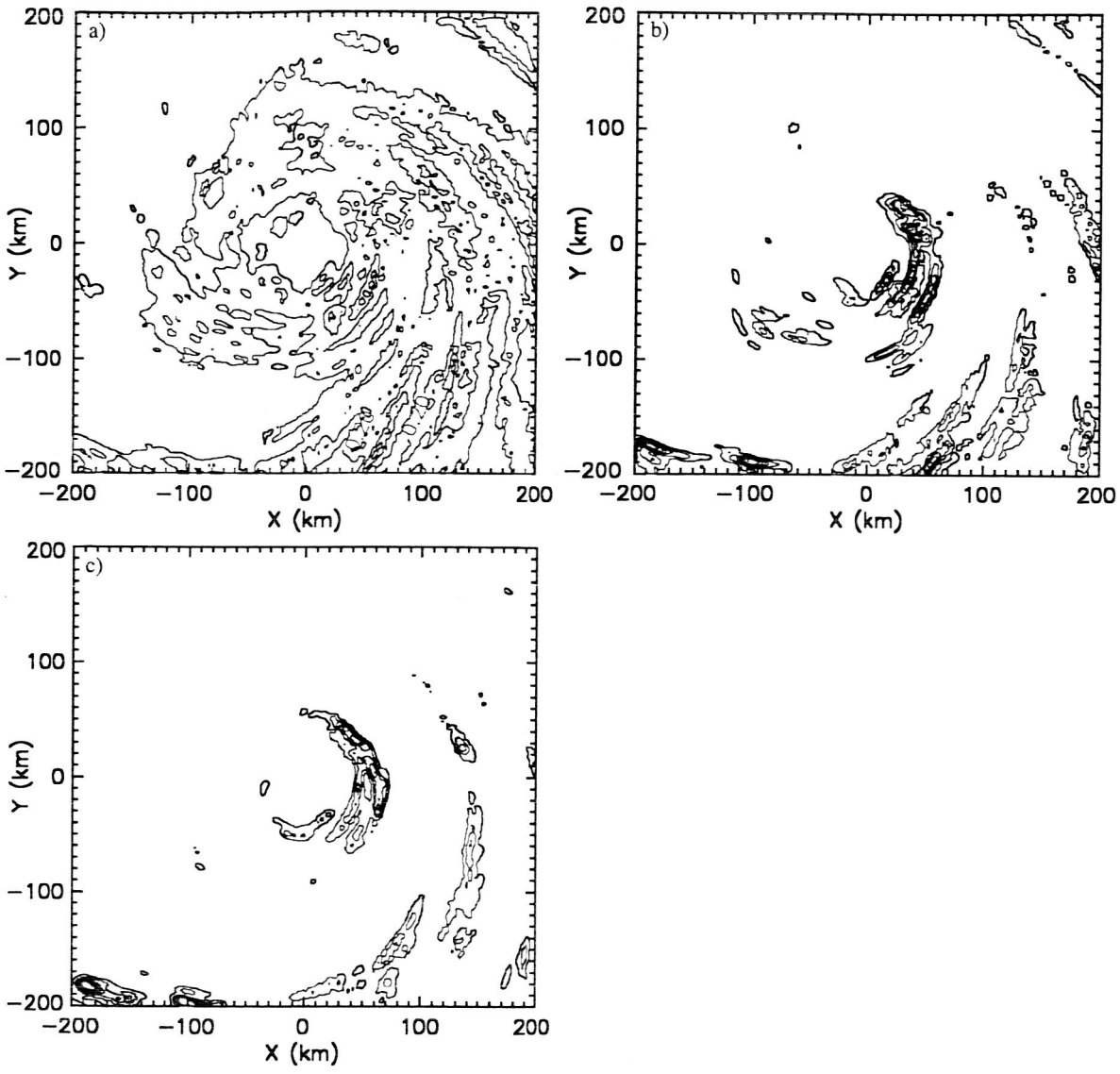

Figure 15. Vertically integrated source terms associated with setting negative mixing ratios to zero for (a) cloud water, (b) rain, and (c) graupel. Contours are drawn at 0.1 g kg^{-1} h^{-1} intervals with light, medium, and dark shading at 0.1, 0.3, and 0.6 g kg^{-1} h^{-1}.